UC San Diego
UC San Diego Electronic Theses and Dissertations

Title
Stochastic modeling of flow and transport in random domains

Permalink
https://escholarship.org/uc/item/62d2k6kk

Author
Park, Sang Woo

Publication Date
2012

Peer reviewed|Thesis/dissertation

UNIVERSITY OF CALIFORNIA, SAN DIEGO

Stochastic Modeling of Flow and Transport in Random Domains

A dissertation submitted in partial satisfaction of the
requirements for the degree
Doctor of Philosophy

in

Engineering Sciences (Aerospace Engineering)

by

Sang Woo Park

Committee in charge:

Professor Daniel M. Tartakovsky, Chair
Professor Marcos Intaglietta
Professor Ratneshwar Lal
Professor Alison L. Marsden
Professor Shankar Subramaniam

2012

The dissertation of Sang Woo Park is approved, and it is

acceptable in quality and form for publication on micro-

film and electronically:

_____

_____

_____

Chair

University of California, San Diego

2012

DEDICATION

To my family.

EPIGRAPH

Learn as if you would live forever; live as if you would die tomorrow

—Mahatma Gandhi

TABLE OF CONTENTS

LIST OF FIGURES

LIST OF TABLES

ACKNOWLEDGEMENTS

Foremost, I would like to express my sincere gratitude to my advisor Prof. Daniel M. Tartakovsky for his continuous support of my Ph.D study and research, for his patience, motivation, enthusiasm, and immense knowledge. His guidance helped me to do my research and to write this thesis. I could not have imagined having a better advisor and mentor for my Ph.D study.

Besides my advisor, I would like to thank Prof. Marcos Intaglietta for his continuous support, guidance and interest in my research.

I would also like to thank to the rest of my thesis committee: Prof. Shankar Subramaniam, Prof. Alison Marsden, and Prof. Ratnesh Lal, for their encouragement and insightful comments.

Last but not least, I would like to thank my family: my mother, my wife, my two daughters, my two brothers and their families, and my in-laws for giving birth to me at the first place and supporting me spiritually throughout my life.

The text of this dissertation includes the reprints of the following papers, either accepted or submitted for consideration at the time of publication. The dissertation author was the primary investigator and author of these publications.

Chapter 1 and 2

C. M. Hightower, B. Y. Salazar Vazquez, S.-W. Park, K. Sriram, J. Martini, O. Yalcin, A. G. Tsai, P. Cabrales, D. M. Tartakovsky, P. C. Johnson and M. Intaglietta

(2011), Integration of cardiovascular regulation by the blood/endothelium cell-free layer. *WIREs Syst. Biol. Med.*, vol. 3, no. 4, doi:10.1002/wsbm.150, pp. 458-470.

Chapter 2

S.-W. Park, M. Intaglietta and D. M. Tartakovsky (2012), Impact of endothelium roughness on blood flow. *J. Theor. Biol., vol. 300, doi:10.1016/j.jtbi.2012.01.017, pp. 152-160.*

<div align="center">VITA</div>

2012	Doctor of Philosophy in Engineering Sciences (Aerospace Engineering), University of California, San Diego.
2008-2012	Graduate Student Researcher, University of California, San Diego.
1996-2006	Researcher, LG(LS) Cable(Machinery), Korea.
1996	Master of Science in Mechanical Engineering , HanYang University, Korea.

<div align="center">JOURNAL PUBLICATIONS</div>

S.-W. Park, M. Intaglietta and D. M. Tartakovsky (2012), Impact of endothelium roughness on blood flow. *J. Theor. Biol., vol. 300, doi:10.1016/j.jtbi.2012.01.017, pp. 152-160.*

C. M. Hightower, B. Y. Salazar Vazquez, S.-W. Park, K. Sriram, J. Martini, O. Yalcin, A. G. Tsai, P. Cabrales, D. M. Tartakovsky, P. C. Johnson and M. Intaglietta (2011), Integration of cardiovascular regulation by the blood/endothelium cell-free layer, WIREs Syst. Biol. Med., vol. 3, no. 4, doi:10.1002/wsbm.150, pp. 458-470.

M. Zayernouri, S.-W. Park, D. M. Tartakovsky, G. E. Karniadakis (2012), Stochastic smoothed profile method for modeling random roughness in flow problems, *Submitted.*

S.-W. Park, M. Intaglietta and D. M. Tartakovsky (2012), Impact of spatio-temporal fluctuations of cell free layer on nitric oxide transport. *In Preparation.*

ABSTRACT OF THE DISSERTATION

Stochastic Modeling of Flow and Transport in Random Domains

by

Sang Woo Park

Doctor of Philosophy in Engineering Sciences (Aerospace Engineering)

University of California, San Diego, 2012

Professor Daniel M. Tartakovsky, Chair

This dissertation deals with mathematical modeling of flow and transport in random domains. Such problems arise when boundaries of simulation domains are either uncertain or fluctuate randomly in time or both. Examples of such problems include flow in micro-channels, micro-fin exchangers, and biological systems. In these and other applications, random domain geometry affects flow and/or transport behavior and heat efficiency.

We use a numerical algorithm consisting of three steps to solve random domain problems with. The first step is to use a finite-term expansion (e.g., a Karhunen-Loéve or Fourier expansion) to parameterize random surfaces (or roughness) of micro-vessels and micro-channels. The second step is to use stochastic mapping, which transforms a deterministic governing equation in a random do-

main into a stochastic equation in a deterministic domain. The final step is to use either a stochastic Galerkin method or a stochastic collocation method to represent a solution of the stochastic equation as polynomial chaos expansions in terms of orthogonal polynomials. The polynomial type is dependent upon the random variable representing the uncertain data/parameter.

This general procedure is used to investigate the effect of endothelial roughness on blood flow, the impact of temporal and spatial fluctuations of cell free layer on nitric oxide production and scavenging, and Stokes flow in domains bounded by surfaces with roughness under a periodic condition.

Chapter 1

Introduction

Numerical and computational models are effective tools for predicting and understanding the behavior of real/practical systems and complex problems. In industrial fields, numerical simulations can provide guidelines for initial product developing and experimentation, leading to reduction in cost and developing time. Though the complex physics in the practical system may be described by numerical and mathematical models, some differences between the model predictions and experiments are unavoidable. That is because models are based on simplifying assumptions/conceptualization and data are prone to experimental and interpretive errors. Therefore, it is important to assess the difference between model predictions and a real phenomenon in order to understand the real physics.

Various sources of uncertainty in physical experiments and numerical simulations stem from the following questions: How to describe a system (a conceptual

model simplified with assumptions)? How to solve numerically the resulting models (finite difference method, finite element method, spectral method, etc.)? How to specify input data/ parameters (geometry, initial and boundary conditions, physical model coefficients, operation conditions, etc.) determining the system. These data/parameters are uncertain in many applications, such as fabrication and assembly processes.

Understanding and assessing the impact of these sources of uncertainty on model predictions is a goal of uncertainty quantification (UQ). UQ is also needed to assess product and process reliability, estimate confidence levels in model predictions, identify relative sources of randomness, and provide robust design solutions capable of handling various operating conditions. This dissertation addresses some of these issues by formulating UQ in a probabilistic/stochastic framework.

In order to solve a stochastic problem accounting for parametric uncertainties, the first step is to treat uncertain inputs as random variables or random processes. By doing this, an original deterministic problem is transformed into a stochastic problem. The latter can be solved by employing a Generalized Polynomial Chaos Expansion (GPCE), which uses orthogonal polynomials to describe random processes [3, 4]. Two popular numerical approaches for UQ, the stochastic Galerkin method (SGM) and a stochastic collocation method (SCM), are described in Appendix A. On the operational level, the key difference between the two methods is that the SGM requires one to modify an existing deterministic solver (intrusive method), which SCM requires no such modifications (nonintrusive

method).

Uncertainty propagation was studied in various In fluid dynamics settings, such as incompressible/compressible flows, thermo fluids, flow with heat transfer in stochastic media, random roughness/contact surface, reacting flows, and fluid-structure interaction problems [5, 6, 7, 8]. The effect of uncertain viscosity on flow and heat transfer in a two-dimensional channel and natural convection in a differentially heated cavity with adiabatic top and bottom walls and cold/hot sidewalls in the Boussinesq limit were investigated in [5, 6]. Uncertainties (such as wind condition, material, manufacturing tolerance) affect the performance of wind turbines, whose predictions require multi-physics (aerodynamics, structural, energy, acoustic) simulations. Design and optimization steps should include a comprehensive estimation of uncertainties in order to achieve robust performance [9, 10].

The focus of this dissertation is on the impact of uncertain (random) geometries on system behavior. Much of the previous research in this area focused on surface roughness. The effects of surface roughness on fluid flow behavior are investigated [11]. It was shown to enhance heat/mass transport for such devices as compact heat exchangers, cooling systems in microelectronics, small bioreactors, oxygenators, microchannel, heat sinks, and micropumps related to heat- and bio-technology.

Another example are surfaces formed by MEMS technologies and manufacturing techniques such as polydimethylsiloxane (PDMS) molding and hydroflouric (HF) etching. Their surface roughness depends upon the fabrication process and

material properties [12, 13]. It affects the performance in the micro systems. Effect of roughness on flow behavior and heat efficiency was investigated in microfluidic systems, such as micro bearing [14, 15], microfins heat exchangers [16], bio-devices [17], and microchannels [18, 19].

Biological systems provide a large number of problems where bounding surfaces are random due to either uncertainty or temporal fluctuations or both. For example, blood vessel walls are lined with endothelium cells and in general are very non-smooth; the inner surface of a cell-free layer is formed by chaotic movement of red blood cells in the vessel's core; etc. The latter surface vary in time and space, and are notoriously hard to image. The impact on blood flow and chemical reactions of random variability of these two surfaces is analyzed in Chapters 2 and 4.

Most early studies of surface roughness employed deterministic methods. This precludes one from incorporating surface measurements and measurement errors into such analyses. By treating these geometries/roughness as random, the problem can be computed. Geometric uncertainties give rise to boundary value problems in random domains. A mapping of random simulation domains onto a deterministic domain transforms a deterministic differential equations into its stochastic counterpart. To solve a problem on a random domain, it is important to parameterize its bounding surface. One such parameterization/representation is provided by Karhunen-Loéve expansions that are related to the correlation function and probability distribution of the random surface [3]. Another representation

of a periodic random process is Fourier expansions [20, 21]. Both of these parameterization strategies are used in this work. We also employ to alternative numerical approaches, the stochastic Galerkin method in Chapters 2 and 3, and the stochastic collocation method in Chapter 4.

1.1 Flow and Transport in Microvessels

We apply the computational tools developed in this research to model blood flow and nitric oxide transport in microcirculation. This setting is ideal because it enables us to explore the effects of random boundaries that are either fixed in time (endothelium surface) or time-varying (the outer layer of the red blood cell–RBC–core). The region between these two surfaces is called a cell free layer (CFL). In cylindrical coordinates its random boundaries are defining by two radii, that of the RBC core R_{RBC} and the inner radius of the endothelial surface R_e (Figure 1.1). Both radii vary in space, i.e., depend on the spatial coordinates (ϕ, z); the RBC column radius R_{RBC} also varies with time t, reflecting chaotic temporal fluctuationss in the CFL width due to intruding RBCs. In other words, $R_e = R_e(\phi, z)$ and $R_e = R_e(\phi, z, t)$.

This spatio-temporal variability, combined with the practical impossibility of measuring the radii values at every space-time point (ϕ, z, t), renders estimates of the radii R_{RBC} and R_e uncertain. This uncertainty propagates through the modeling process, affecting predictions of key physiological quantities such as wall

shear stress, effective blood viscosity, and delineation of barriers to oxygen and nitric oxide transport. The uncertainty is quantified by treating the radii R_{RBC} and R_e as random fields, which vary not only in physical space (ϕ, z) and time t, but also in the probability space $\omega \in \Omega$. The latter space consists of the collection of all possible realizations of the random radii R_{RBC} and R_e. Thus, $R_e = R_e(\phi, z, \omega)$ and $R_e = R_e(\phi, z, t, \omega)$.

The randomness of R_{RBC} and R_e affects the modeling process since flow and transport processes in the CFL are now defined by equations (e.g., Stokes equations for flow and advection-reaction-diffusion equations for transport) that must be solved on the domain bounded by these random boundaries. Analysis of this problem is facilitated by the use of stochastic mappings, an approach that has been promulgated in a series of recent papers [22, 23, 20]. The basic idea of this approach is to map a random domain onto its deterministic counterpart. In the present context, this is accomplished by transforming the (r, ϕ, z) coordinate system associated with the random boundaries of the CFL into the (ξ_1, ξ_2, ξ_3) coordinate system, such that $\xi_1 = (r - R_{RBC})/(R_e - R_{RBC})$, $\xi_2 = \phi$, and $\xi_3 = z$. While the radius r varies between the two random limits, $R_{RBC}(\phi, z, t, \omega) \leq r \leq R_e(\phi, z, \omega)$, the transformed variable ξ_1 is defined on the deterministic interval $0 \leq \xi_1 \leq 1$.

Since the transformation Jacobian $J(\xi_1, \xi_2, \xi_3, \omega) = \partial(r, \phi, z)/\partial(\xi_1, \xi_2, \xi_3)$ is random, the transformed flow and/or transport equations become stochastic. Since the theory of stochastic differential equations defined on deterministic domains is

relatively mature, one can use a variety of well-established techniques, including perturbation expansions [22], polynomial chaos expansions [23], and stochastic collocation methods [24].

Random variability of the CFL boundaries can significantly affect the physiological phenomena taking place in the CFL. For example, a classical treatment of blood flow in arteries whose walls are modeled as smooth surfaces of radii R relies on the Poiseuille law to relate volumetric flow rate Q to pressure gradient dp/dz (pressure drop along the blood vessel divided by its length),

$$Q = -\frac{\pi R^4}{8\mu}\frac{dp}{dz} \tag{1.1}$$

where μ is the dynamic blood viscosity of blood. For flow in vessels with rough walls, this expression is phenomenologically modified,

$$Q = -\frac{\pi R^4 C_L}{8\mu}\frac{dp}{dz}, \tag{1.2}$$

where C_L is the Lomize roughness coefficient [25]. Depending on the degree of wall roughness, the reliance on the standard Poiseuille law can yield estimates of the blood viscosity that are as much as 20% lower.

Since the Lomize roughness coefficient C_L is largely phenomenological, its values for different vessel radii cannot be ascertained with certainty, and measurements of the CFL topology (i.e., observations of R_{RBC} and R_e) cannot be readily incorporated to improve estimates of C_L. The stochastic framework overcomes these limitations by both providing a theoretical foundation for the concept of the Lomize roughness coefficient and facilitating data processing by using data to

estimate statistical properties (e.g., means, variances, and space-time correlation functions) of the random fields R_{RBC} and R_e.

Random variability of these surfaces also affects the production and scavenging of nitric oxide (NO), which plays an important role in relaxing the smooth muscle. The NO distribution in microcirculation depends on mechanical characteristics of blood flow, such as wall shear stress, radial velocity profile, hematocrit, and the CFL width. This problem is studied in Chapter 4.

1.2   Governing Equations

Using the Einstein summation notation, the mass conservation (continuity) equation can be written as

$$\frac{\partial \rho}{\partial t} + \frac{\partial (\rho u_i)}{\partial x_i} = 0, \tag{1.3}$$

where ρ is the blood viscosity, u_i $(i = 1, 2, 3)$ are the components of the velocity vector $\mathbf{u}$. The momentum conservation equation is

$$\rho \left(\frac{\partial u_i}{\partial t} + u_j \frac{\partial u_i}{\partial x_j} \right) = \frac{\partial \sigma_{ij}}{\partial x_j}, \tag{1.4}$$

where σ_{ij} $(i, j = 1, 2, 3)$ are components the stress tensor $\boldsymbol{\sigma}$ defined as

$$\sigma_{ij} = -p\delta_{ij} + \tau_{ij}, \qquad \tau_{ij} = \mu \left(\frac{\partial u_j}{\partial x_i} + \frac{\partial u_i}{\partial x_j} \right) \tag{1.5}$$

where p is pressure, and τ_{ij} $(i, j = 1, 2, 3)$ are components of the deviatoric stress tensor $\boldsymbol{\sigma}$. For steady, two-dimensional, incompressible, low Reynolds/film flow,
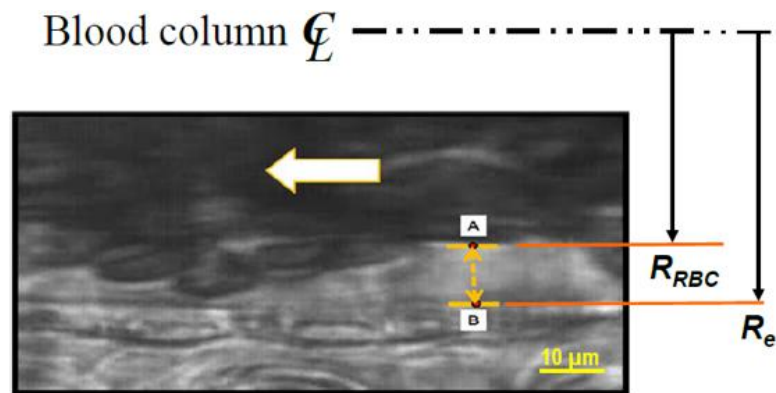
Figure 1.1: Cell free plasma layer (CFL) in vivo. Image of an arteriolar wall showing CFL width, the distance between the RBC column (black) and the endothelium lining the vessel wall. This image shows a few RBCs positioned closer to the endothelium. CFL width is the distance between A and B. RBCs are 7 m in diameter. Blood flow is from right to left (arrow) [1].

the momentum equation is given by

$$\frac{\partial p}{\partial x} = \frac{\partial \tau_{xx}}{\partial x} + \frac{\partial \tau_{xy}}{\partial y}, \qquad \frac{\partial p}{\partial y} = \frac{\partial \tau_{xy}}{\partial x} + \frac{\partial \tau_{yy}}{\partial y}, \tag{1.6}$$

$$\tau_{xx} = 2\mu \frac{\partial u}{\partial x}, \qquad \tau_{xy} = \mu \left(\frac{\partial u}{\partial y} + \frac{\partial v}{\partial x} \right), \qquad \tau_{yy} = 2\mu \frac{\partial v}{\partial y}. \tag{1.7}$$

These equations are used in Chapters 2 and 3 to model Stokes flows in vessels with random walls. They are general enough to handle two-phase fluids separated by a random interface. When combined with the continuity equation, the Stokes equations become

$$\frac{\partial p}{\partial x} = \mu \left(\frac{\partial^2 u}{\partial x^2} + \frac{\partial^2 u}{\partial y^2} \right), \qquad \frac{\partial p}{\partial y} = \mu \left(\frac{\partial^2 v}{\partial x^2} + \frac{\partial^2 v}{\partial y^2} \right). \tag{1.8}$$

In physical spaces, we have used spectral collocation method and spectral element method [26, 27, 28, 29]. In chapter 2, these equations are solved by using the spectral method in which the solution expanded in a series of orthogonal basis functions put into the differential equations and the coefficients of expansion is obtained with collocation. In chapter 3 and 4 the spectral element method is used in physical spaces . This spectral element method is described in Appendix C.

Chapter 2

Flow over Random Wall

2.1 Introduction

The distribution of nitric oxide (NO) in the microcirculation is determined, in large part, by the balance between NO production and consumption in the blood and tissue compartments. A key mechanism of this balance is the gradient of NO concentration at the interface between blood and tissue, a complex submicroscopic region generally free of red blood cells (RBCs). It is termed the "cell free layer" (CFL). The CFL is bounded by the surface of the endothelium and the surface of the moving RBC column, a configuration that can be modeled as a two layer system. Analysis of this model can be approximated by assuming a Newtonian fluid and a parabolic profile velocity within the CFL which mergers into plug flow and non-Newtonian flow properties in the central RBC core [30, 31]. Several studies used this approach to estimate the velocity gradient in the CFL and

to estimate shear stress at the vessel wall. The level of shear stress determines the rate of NO production by the endothelium [1]. The width of the CFL modulates the rate of NO scavenging by RBCs, since it determines the distance from the source of NO to its major sink on the blood side [32, 33, 31, 34].

Shear stress is determined by the effective viscosity, the velocity gradient, the nature of the flow and the flow boundary geometry. NO bioavailability and oxygen transfer is determined by the shear stress, flow conditions, hematocrit (Hct) and the CFL width. The relation between NO production and shear stress has been analyzed experimentally and theoretically [35, 36]. Theoretical studies reveal that the CFL width and shear stress are primary factors in determining NO bioavailability in the vessel wall [37]. These studies assume that the interface between the RBC column and plasma is a smooth deterministic surface. However this surface is formed by RBC that deform and aggregate forming an irregular boundary [38, 39], affecting flow and shear stress on the endothelium. Likewise, the endothelium surface exhibits (random) spatial variability.

The endothelium is exposed to a flow field that transmits a distribution of shear stresses to its surface. These forces have a heterogeneous spatial distribution evidenced by the difference of response levels even in contiguous cells are often noted in neighboring cells. This variability was proposed [40] to be in part the consequence of the cell surface geometry. The latter was quantified in living endothelium by means of atomic force microscopy measurements [41].

A deterministic characterization of this undulating surface [42], which treated

its profile as a sinusoid, relied on two parameters: the length in flow direction divided by the width transverse to flow, and the height-to-length ratio. These parameters were used to determine the maximum shear stress and shear stress gradient developed by flow by mean of an analytic linearized solution to the governing equations. The analysis in [42] revealed that shear stress gradients at the surface of the endothelium are very large, a consequence of the small dimension over which changes occur.

The topographic variability of the endothelial surface is not well established, rendering their deterministic descriptions problematic. It is known that the endothelial surface is affected by both blood flow and the physiological condition. Various factors, such as endothelial swelling and dehydration [43] and endothelial contractility [44], are modulators of the surface topography that remain unexplored. The study [41] showed that flow also changes the surface from a smooth and uniform sinusoid-like variation to the appearance of fibrous structures embedded in the surface. Such a variety of features suggests that the surface be described by means of stochastic variables and treated as a random boundary characterized by a correlation length (of its variability) in the direction of flow, a mean perturbation height and a standard deviation of this mean height.

Spatial variability of the CFL width is highly uncertain [38, 39]. To quantify the impact of this uncertainty on measured and observed flow characteristics (e.g., shear stress on endothelium walls), we treat the CFL surface as a random field. A problem formulation, which describes blood flow in a flow chamber with

randomly varying aperture, is presented in Section 2.2. In Section 2.3 we use a Karhunen-Loève expansion [45] as a means of statistical parameterization of this random boundary. A numerical algorithm for solving the Stokes flow equations in the resulting random domain is described in Section 2.4. It follows a procedure introduced in [22, 20, 23] and consists of two steps. First, the random flow domain is mapped onto a deterministic domain with smooth boundaries (Section 2.4.1), the transformed Stokes equations become stochastic. Second, a generalized polynomial chaos expansion [4] is used in Section 2.4.3 to solve these equations. Biophysical implications of our analysis are discussed in detail in Section 2.5 and summarized in Section 2.6.

2.2 Problem Formulation

Consider viscous (low Reynolds number) steady-state blood flow between two plates, one of which is smooth (deterministic) and the other is rough (random). Let μ denote the kinematic viscosity of blood. Then flow velocity $\mathbf{u} = (u_1, u_2)^T$ and pressure distribution p at every point $\mathbf{x}$ in the flow domain $\mathcal{D}$ are governed by the Stokes and continuity equations,

$$\mu \nabla^2 \mathbf{u} = \nabla p, \qquad \nabla \cdot \mathbf{u} = 0, \qquad \mathbf{x} \in \mathcal{D}. \tag{2.1}$$

The lower boundary, $s(x_1)$, of the flow domain $\mathcal{D} = \{(x_1, x_2) : 0 \leq x_1 \leq L_x, s(x_1) \leq x_2 \leq L_y\}$ is uncertain. This uncertainty is conceptualized by allowing s to vary randomly in space, i.e., by treating it as a random field $s(x_1, \omega)$ where

$\omega \in \Omega$ indicates a realization ("coordinate") in probability space Ω. A typical realization of the random flow domain $\mathcal{D}(\omega)$ is shown in Figure 2.3a below.

The flow is driven by an externally imposed pressure gradient, such that

$$p(0, x_2) = P_l, \qquad p(L_x, x_2) = P_r, \qquad s \leq x_2 \leq L_y. \tag{2.2a}$$

The normal components of the pressure gradient on the two walls is zero,

$$\mathbf{n} \cdot \nabla p(x_1, s) = 0, \qquad \frac{\partial p}{\partial x_2}(x_1, L_y) = 0. \tag{2.2b}$$

We assume the lower and upper plates to be impermeable,

$$\mathbf{n} \cdot \mathbf{u}(x_1, s) = 0, \qquad v(x_1, L_y) = 0, \tag{2.3a}$$

and impose no-slip boundary conditions,

$$\mathbf{s} \cdot \mathbf{u}(x_1, s) = 0, \qquad u(x_1, L_y) = 0. \tag{2.3b}$$

Here $\mathbf{n}$ and $\mathbf{s}$ denote the unit normal and tangential vectors to the random surface $s(x_1, \omega)$, respectively.

2.3 Statistical Representation of Random Surfaces

Let us employ the Reynolds decomposition, $s(x_1, \omega) = \bar{s}(x_1) + s'(x_1, \omega)$, to represent the random surface $s(x_1, \omega)$ as the sum of its ensemble mean $\bar{s}(x_1)$ and zero-mean fluctuations $s'(x_1, \omega)$ about this mean. We assume that available

data, such as those reported in [39], are sufficient to estimate the relevant statistics of $s(x_1, \omega)$, including its mean $\bar{s}$, standard deviation σ_s, and a two-point correlation function $\rho_s(x_1, y_1)$. Then the random field $s(x_1, \omega)$ can be represented via a Karhunen-Loève expansion,

$$s(x_1, \omega) = \bar{s}(x_1) + \sigma_s \sum_{m=1}^{\infty} \sqrt{\lambda_m} f_m(x_1) Y_m(\omega). \tag{2.4}$$

Here $Y_m(\omega)$ ($m \geq 1$) are independent random variables, and λ_m and $f_m(x_1)$ are eigenvalues and eigenfunctions of Fredholm equations,

$$\int_0^{L_x} \rho_s(x_1, y_1) f_m(y_1) \mathrm{d}y_1 = \lambda_m f_m(x_1), \qquad m \geq 1. \tag{2.5}$$

For an exponential correlation function,

$$\rho_s(x_1, y_1) = \mathrm{e}^{-|x_1 - y_1|/l_s} \tag{2.6}$$

with the correlation length $l_s > 0$, the eigenvalue problem in Eq. 2.5 admits an analytical solution [24],

$$\lambda_m = \frac{2l_s}{l_s^2 \omega_m^2 + 1}, \qquad m \geq 1 \tag{2.7}$$

and

$$f_m(x) = \frac{1}{\sqrt{(l_s^2 \omega_m^2 + 1)L_x/2 + l_s}} [l_s \omega_m cos(\omega_m x) + sin(\omega_m x)] \tag{2.8}$$

where ω_m in Eqs. 2.7 and 2.8 are solutions of

$$(l_s^2 \omega_m^2 - 1) sin(\omega_m L_x) = 2l_s \omega_m cos(\omega_m L_x). \tag{2.9}$$

Practical implementation of Karhunen-Loève expansions requires one to truncate the infinite summation in Eq. 2.4. The resulting truncation error depends

on the correlation length l_s. The larger the correlation length, the few terms in Eq. 2.4 are necessary to represent the random surface $s_1(x_1, \omega)$ with a given degree of accuracy. Figure 2.1 shows how the decreasing correlation lengths l_s affect the decay of the eigenvalues λ_m for the exponential correlation function in Eq. 2.6.

Within the statistical framework adopted here, the endothelium roughness is characterized by two parameters: the standard deviation σ_s and the correlation length l_s. Typical realizations of the uncertain (random) endothelium surface $s(x_1, \omega)$ for several values of standard deviation σ_s and correlation length l_s are shown in Figure 2.2.

2.4 Solving Stokes Equations on Random Domain

A two-step approach to solving differential equations on random (uncertain) domains is described and implemented below.

2.4.1 Stochastic mapping onto a deterministic domain

Let us introduce a new coordinate system (ξ_1, ξ_2), in which the original stochastic flow domain $\mathcal{D}$ takes the form of a deterministic rectangle $E = \{(\xi_1, \xi_2) : 0 \leq \xi_1 \leq L_x, 0 \leq \xi_2 \leq L_y\}$. A mapping $\mathcal{D} \rightarrow E$ is accomplished by a transformation of coordinates $\xi_i = \xi_i(x_1, x_2)$ $(i = 1, 2)$. For the relatively simple flow domain under consideration, such a mapping can be defined analytically, for example, as
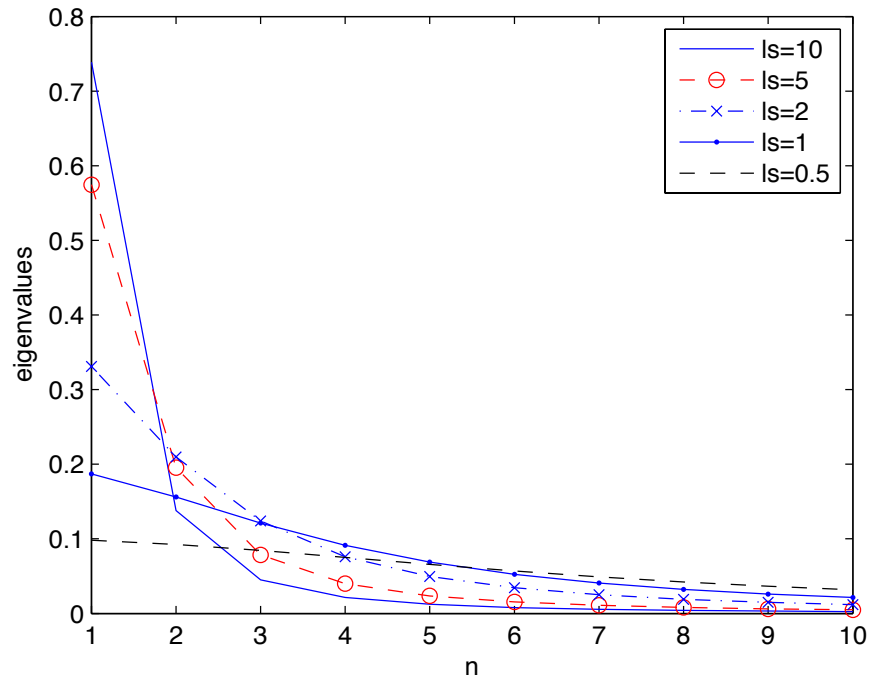
Figure 2.1: Decay of eigenvalues λ_n with n for several correlation lengths l_s.
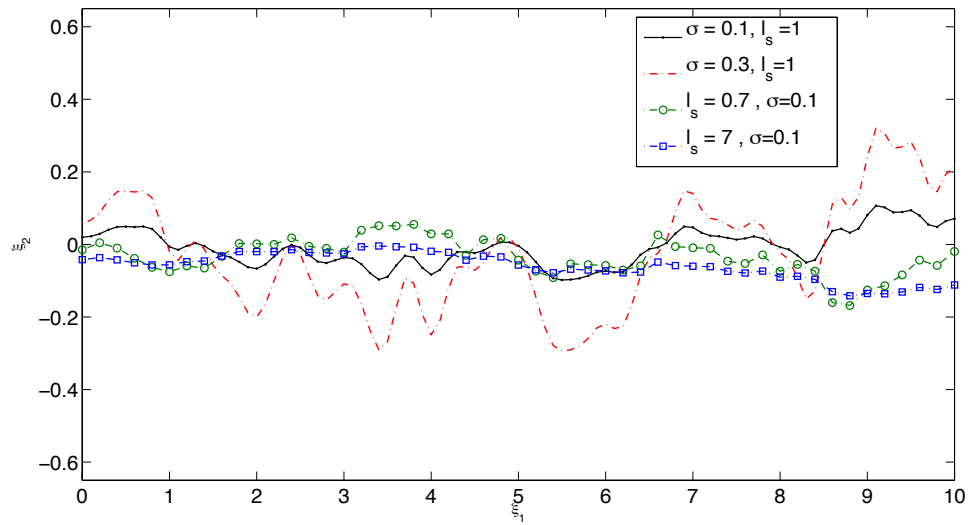
Figure 2.2: Typical realizations of the uncertain (random) endothelium surface $s(x_1, \omega)$ for several values of standard deviation σ_s and correlation length l_s.

$\xi_1 = x_1$ and $\xi_2 = (L_y - x_2)/[L_y - s(x_1, \omega)]$. For more complex geometries, a stochastic mapping $\xi_i = \xi_i(x_1, x_2)$ ($i = 1, 2$) and its inverse $x_i = x_i(\xi_1, \xi_2)$ ($i = 1, 2$) are constructed [22, 23] by solving Laplace's equations,

$$\frac{\partial^2 x_i}{\partial \xi_1^2} + \frac{\partial^2 x_i}{\partial \xi_2^2} = 0, \quad (\xi_1, \xi_2) \in E, \quad i = 1, 2. \tag{2.10}$$

subject to the boundary conditions

$$x_1(0, \xi_2) = 0, \quad x_1(L_x, \xi_2) = L_x, \quad x_1(\xi_1, 0) = \xi_1, \quad x_1(\xi_1, L_y) = \xi_1; \tag{2.11a}$$

$$x_2(0, \xi_2) = \xi_2, \quad x_2(L_x, \xi_2) = \xi_2, \quad x_2(\xi_1, 0) = s, \quad x_2(\xi_1, L_y) = L_y. \tag{2.11b}$$

Uncertainty (randomness) in domain geometry, $s(x_1, \omega)$, manifests itself in the mapping problem through a boundary condition in Eqs. 2.11. To facilitate numerical solution of the mapping problem given by Eqs. 2.10–2.11, one has to truncate the infinite series in the Karhunen-Loève expansion (2.4) after K terms. For a given accuracy, the smaller the correlation length l_s, the higher the value of K [see, e.g.,[4, 23]].

Solutions of Eqs. 2.10–2.11 can now be approximated by series

$$x_i(\xi_1, \xi_2, \omega) = \sum_{k=0}^{K} \hat{x}_{i,k}(\xi_1, \xi_2) Y_k(\omega), \quad i = 1, 2. \tag{2.12}$$

Substituting Eq. 2.12 into Eq. 2.10 and taking a Galerkin projection yields $2(K+1)$ Laplace's equations for the coefficients $\hat{x}_{i,k}(\xi_1, \xi_2)$,

$$\frac{\partial^2 \hat{x}_{i,k}}{\partial \xi_1^2} + \frac{\partial^2 \hat{x}_{i,k}}{\partial \xi_2^2} = 0, \quad (\xi_1, \xi_2) \in E, \quad i = 1, 2, \quad k = 0, \ldots, K. \tag{2.13}$$

For $k = 0$, Eqs. 2.13 are subject to boundary conditions

$$x_{1,0}(0, \xi_2) = 0, \quad x_{1,0}(L_x, \xi_2) = L_x, \quad x_{1,0}(\xi_1, 0) = \xi_1, \quad x_{1,0}(\xi_1, L_y) = \xi_1; \quad (2.14\text{a})$$

$$x_{2,0}(0, \xi_2) = \xi_2, \quad x_{2,0}(L_x, \xi_2) = \xi_2, \quad x_{2,0}(\xi_1, 0) = \overline{s}, \quad x_{2,0}(\xi_1, L_y) = L_y. \quad (2.14\text{b})$$

For $k \geq 1$, these boundary conditions are replaced with their homogeneous coun-

terparts,

$$x_{1,k}(0, \xi_2) = 0, \quad x_{1,k}(L_x, \xi_2) = 0, \quad x_{1,k}(\xi_1, 0) = 0, \quad x_{1,k}(\xi_1, L_y) = 0; \quad (2.14\text{c})$$

$$x_{2,k}(0, \xi_2) = 0, \quad x_{2,k}(L_x, \xi_2) = 0, \quad x_{2,k}(\xi_1, L_y) = 0, \quad (2.14\text{d})$$

except for the boundary conditions

$$x_{2,k}(\xi_1, 0) = \sigma_s \sqrt{\lambda_k} \psi_k(\xi_1). \quad (2.14\text{e})$$

We use a Chebyshev spectral method to solve Eqs. 2.13–2.14. An example of

such calculations is shown in Figure 2.3 for one realization of the random surface

$s(x_1, \omega)$.

2.4.2 Transformed Stokes equations

The procedure outlined above enables one to compute, among other things,

a transformation Jacobian,

$$J(\xi_1, \xi_2, \omega) \equiv \frac{\partial(\xi_1, \xi_2)}{\partial(x_1, x_2)} = J[\xi_1, \xi_2, Y_1(\omega), \cdots, Y_K(\omega)]. \quad (2.15)$$

For an arbitrary twice-differentiable function $f(\mathbf{x})$ defined on $\mathcal{D}$,

$$\nabla_{\mathbf{x}}^2 f \equiv \nabla_{\mathbf{x}} \cdot \mathbf{F} = \frac{1}{J}\left(\frac{\partial F^1}{\partial \xi_1} + \frac{\partial F^2}{\partial \xi_2}\right) \equiv \frac{1}{J}\nabla_{\boldsymbol{\xi}} \cdot \mathbf{F}, \quad (2.16\text{a})$$
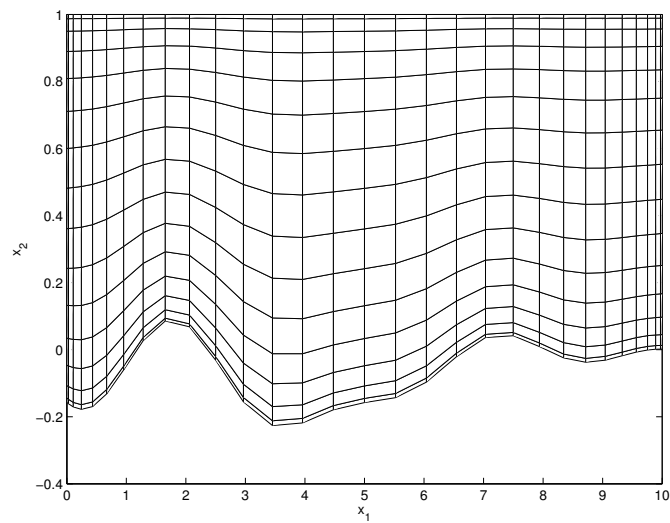
(a)
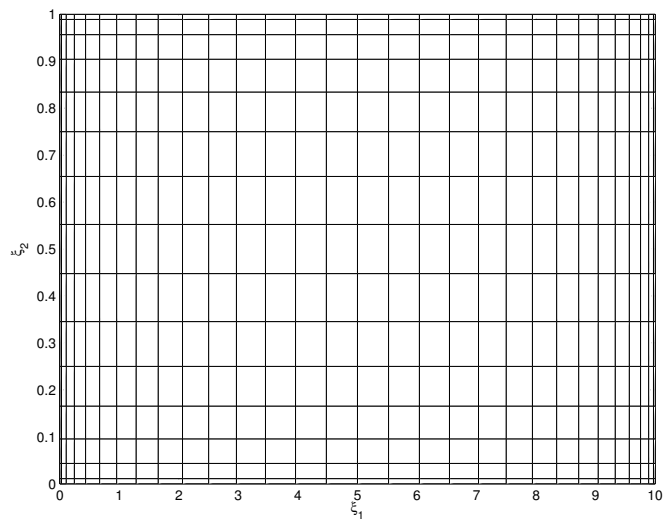
(b)

Figure 2.3: (a) A typical realization of the random flow domain $\mathcal{D}(\omega)$ and (b) its mapping onto a deterministic domain.

$$\nabla_{\mathbf{x}} f = \frac{1}{J} \left[\left(\frac{\partial x_2}{\partial \xi_2} \mathbf{i} - \frac{\partial x_1}{\partial \xi_2} \mathbf{j} \right) \frac{\partial f}{\partial \xi_1} - \left(\frac{\partial x_2}{\partial \xi_1} \mathbf{i} - \frac{\partial x_1}{\partial \xi_1} \mathbf{j} \right) \frac{\partial f}{\partial \xi_2} \right]. \tag{2.16b}$$

where $\mathbf{i}$ and $\mathbf{j}$ are the normal vectors of the (ξ_1, ξ_2) coordinate system, and the contravariant components F^1 and F^2 of the transformed vector $\mathbf{F}(\boldsymbol{\xi})$ are given by

$$F^1 = A \frac{\partial f}{\partial \xi_1} - B \frac{\partial f}{\partial \xi_2}, \qquad F^2 = -B \frac{\partial f}{\partial \xi_1} + C \frac{\partial f}{\partial \xi_2} \tag{2.16c}$$

with

$$A = \frac{1}{J} \left[\left(\frac{\partial x_2}{\partial \xi_2} \right)^2 + \left(\frac{\partial x_1}{\partial \xi_2} \right)^2 \right], \qquad B = \frac{1}{J} \left(\frac{\partial x_2}{\partial \xi_1} \frac{\partial x_2}{\partial \xi_2} + \frac{\partial x_1}{\partial \xi_1} \frac{\partial x_1}{\partial \xi_2} \right),$$

$$C = \frac{1}{J} \left[\left(\frac{\partial x_2}{\partial \xi_1} \right)^2 + \left(\frac{\partial x_1}{\partial \xi_1} \right)^2 \right]. \tag{2.16d}$$

Using Eqs. 2.16 to rewrite the Stokes Eqs. 2.1 in the (ξ_1, ξ_2) coordinate system, we obtain

$$\frac{\partial}{\partial \xi_1} \left(A \frac{\partial u_1}{\partial \xi_1} - B \frac{\partial u_1}{\partial \xi_2} \right) - \frac{\partial}{\partial \xi_2} \left(B \frac{\partial u_1}{\partial \xi_1} - C \frac{\partial u_1}{\partial \xi_2} \right) = \frac{1}{\mu} \left(\frac{\partial x_2}{\partial \xi_2} \frac{\partial p}{\partial \xi_1} - \frac{\partial x_2}{\partial \xi_1} \frac{\partial p}{\partial \xi_2} \right) \tag{2.17a}$$

and

$$\frac{\partial}{\partial \xi_1} \left(A \frac{\partial u_2}{\partial \xi_1} - B \frac{\partial u_2}{\partial \xi_2} \right) - \frac{\partial}{\partial \xi_2} \left(B \frac{\partial u_2}{\partial \xi_1} - C \frac{\partial u_2}{\partial \xi_2} \right) = \frac{1}{\mu} \left(\frac{\partial x_1}{\partial \xi_2} \frac{\partial p}{\partial \xi_2} - \frac{\partial x_1}{\partial \xi_2} \frac{\partial p}{\partial \xi_1} \right). \tag{2.17b}$$

The Stokes and continuity Eqs. 2.1 imply that $\nabla_{\mathbf{x}}^2 p = 0$. When written in the (ξ_1, ξ_2) coordinate system, this equation takes the form

$$\frac{\partial}{\partial \xi_1} \left(A \frac{\partial p}{\partial \xi_1} - B \frac{\partial p}{\partial \xi_2} \right) - \frac{\partial}{\partial \xi_2} \left(B \frac{\partial p}{\partial \xi_1} - C \frac{\partial p}{\partial \xi_2} \right) = 0. \tag{2.18}$$

The transformed flow Eqs. 2.16–2.18 are stochastic, i.e., have random coefficients. The theory of stochastic differential equations defined on deterministic

domains is relatively mature. Their solutions can be obtained with a variety of well-established techniques, including perturbation-based moment equations [46], stochastic finite elements [3], and stochastic collocation methods [24, and the references therein]. In the subsequent numerical simulations we employ a stochastic finite element method, which is also known as the generalized polynomial chaos expansion [23].

2.4.3 Solution of stochastic flow equations

Let $\{\Psi_m(\mathbf{Y})\}_{m=0}^M$ denote a set of multidimensional orthogonal polynomials of the random vector $\mathbf{Y}(\omega) \equiv (Y_1, \ldots, Y_K)^T$ of the K independent random variables $Y_1(\omega), \ldots, Y_K(\omega)$ introduced in Eqs. 2.4 and 2.12. The polynomials are chosen to have the ensemble means $\overline{\Psi}_0 = 1$ and $\overline{\Psi}_k = 0$ ($k \geq 1$) and satisfy the orthogonality condition

$$\overline{\Psi_i \Psi_j} = \overline{\Psi_i^2} \delta_{ij}, \qquad \overline{\Psi_i \Psi_j} \equiv \int \Psi_i(\mathbf{Y}) \Psi_j(\mathbf{Y}) W(\mathbf{Y}) \mathrm{d}Y_1 \ldots \mathrm{d}Y_K, \qquad (2.19)$$

where δ_{ij} is the Kronecker delta and $W(\mathbf{Y})$ is a weight function corresponding to a given polynomial type.

The size of the polynomial set, M, is determined by the "stochastic dimension" K and the order P of polynomials Ψ_k, according to

$$M = \frac{(K+P)!}{K!P!} - 1. \qquad (2.20)$$

Polynomial chaos expansions (PCEs) represent a system state, e.g., pressure $p(\boldsymbol{\xi}, \omega)$,

a random field whose ensemble statistics are to be determined, as a series

$$p(\boldsymbol{\xi}, \omega) = \sum_{k=0}^{M} \hat{p}_k(\boldsymbol{\xi}) \Psi_k[\mathbf{Y}(\omega)]. \tag{2.21}$$

Similar expansions are employed for the other two state variables, $u_1(\boldsymbol{\xi}, \omega)$ and $u_2(\boldsymbol{\xi}, \omega)$ and metrics coefficients, $A(\boldsymbol{\xi}, \omega)$, $B(\boldsymbol{\xi}, \omega)$ and $C(\boldsymbol{\xi}, \omega)$. Following the Galerkin projection procedure outlined in the Appendix A.1, we obtain a set of deterministic equations for the coefficients $\{\hat{p}_k(\boldsymbol{\xi})\}_{k=0}^{M}$, $\{\hat{u}_{1k}(\boldsymbol{\xi})\}_{k=0}^{M}$ and $\{\hat{u}_{2k}(\boldsymbol{\xi})\}_{k=0}^{M}$,

$$\sum_{j,k=0}^{M} \mathcal{C}_{ijk} \left[\frac{\partial}{\partial \xi} \left(\hat{A}_k \frac{\partial \hat{u}_j}{\partial \xi} - \hat{B}_k \frac{\partial \hat{u}_j}{\partial \eta} \right) + \frac{\partial}{\partial \eta} \left(\hat{C}_k \frac{\partial \hat{u}_j}{\partial \eta} - \hat{B}_k \frac{\partial \hat{u}_j}{\partial \xi} \right) \right]$$
$$= \frac{1}{\mu} \sum_{j,k=1}^{M} \mathcal{C}_{ijk} \left(\hat{D}_k \frac{\partial \hat{p}_j}{\partial \xi} - \hat{E}_k \frac{\partial \hat{p}_j}{\partial \eta} \right) \tag{2.22}$$

$$\sum_{j,k=0}^{M} \mathcal{C}_{ijk} \left\{ \frac{\partial}{\partial \xi} \left(\hat{A}_k \frac{\partial \hat{v}_j}{\partial \xi} - \hat{B}_k \frac{\partial \hat{v}_j}{\partial \eta} \right) + \frac{\partial}{\partial \eta} \left(\hat{C}_k \frac{\partial \hat{v}_j}{\partial \eta} - \hat{B}_k \frac{\partial \hat{v}_j}{\partial \xi} \right) \right\}$$
$$= \frac{1}{\mu} \sum_{j,k=0}^{M} \mathcal{C}_{ijk} \left(-\hat{F}_k \frac{\partial \hat{p}_j}{\partial \xi} + \hat{G}_k \frac{\partial \hat{p}_j}{\partial \eta} \right) \tag{2.23}$$

$$\sum_{j,k=0}^{M} \mathcal{C}_{ijk} \left\{ \left(\hat{D}_k \frac{\partial \hat{u}_j}{\partial \xi} - \hat{E}_k \frac{\partial \hat{u}_j}{\partial \eta} \right) + \left(-\hat{F}_k \frac{\partial \hat{v}_j}{\partial \xi} + \hat{G}_k \frac{\partial \hat{v}_j}{\partial \eta} \right) \right\} = 0 \tag{2.24}$$

$$\sum_{j,k=0}^{M} \mathcal{C}_{ijk} \left[\frac{\partial}{\partial \xi} \left(\hat{A}_k \frac{\partial \hat{p}_j}{\partial \xi} - \hat{B}_k \frac{\partial \hat{p}_j}{\partial \eta} \right) + \frac{\partial}{\partial \eta} \left(\hat{C}_k \frac{\partial \hat{p}_j}{\partial \eta} - \hat{B}_k \frac{\partial \hat{p}_j}{\partial \xi} \right) \right] = 0. \tag{2.25}$$

Here $\mathcal{C}_{ijk} \equiv \overline{\Psi_i \Psi_j \Psi_k}$, $A = \sum_{k}^{M} \hat{A}_k \Psi_k$, and $\hat{B}_k$, $\hat{C}_k$, $\hat{D}_k$, $\hat{E}_k$, $\hat{F}_k$, $\hat{G}_k$ are coefficients in the similar expansions of B, C, D, E, F, and G, respectively.

Algebraic Eqs. 2.22–2.25 were solved by using a spectral collocation method.

2.5 Simulation Results and Discussion

Algebraic Eqs. 2.22–2.25 were solved by using a spectral collocation method. Then, the mean $\bar{p}(\mathbf{x})$ and variance $\sigma_p^2(\mathbf{x})$ of pressure $p(\boldsymbol{\xi}, \omega)$ are computed as

$$\bar{p}(\mathbf{x}) = p_0(\mathbf{x}), \qquad \sigma_p^2(\mathbf{x}) = \sum_{k=1}^{M} p_k^2(\mathbf{x}) \overline{\Psi_k^2}. \tag{2.26}$$

The identical procedure are used to compute the means and variances of the velocity components $u_1(\boldsymbol{\xi}, \omega)$ and $u_2(\boldsymbol{\xi}, \omega)$. These means and variances serve to predict respectively the average behavior of, and to quantify predictive uncertainty for, blood pressure and velocity (Section 2.5.1) and shear stress on the endothelium (Section 2.5.2). In Section 2.5.3 we investigate the impact of endothelium roughness on the estimation of effective blood viscosity.

2.5.1 Blood pressure and velocity

Figure 2.4 exhibits the statistics of pressure resultant from uncertain geometry of the endothelium wall $s(x_1)$. The mean pressure $\bar{p}$ in Figure 2.4a decreases linearly from left to right between two pressure values imposed on the inlet and outlet of the flow chamber. In other words, the mean pressure gradient is constant and unaffected by the endothelium roughness. The uncertain geometry of the endothelium manifests itself in pressure fluctuations about the mean, as quantified by the standard deviation σ_p in Figure 2.4b. Predictive uncertainty increases with the distance from the inlet and outlet, where pressure is certain, reaching its maximum in the middle of the flow chamber ($\xi_1 = L_x/2$). It also decreases with the

distance from the uncertain endothelium surface ($\xi_2 = 0$).

Figure 2.5 highlights these observations further by presenting several cross-sections of the standard deviation of pressure σ_p. In particular, it reveals the dependence of σ_p on the distance from the uncertain endothelium surface is relatively mild (Figure 2.5b). This dependence becomes more pronounced as the degree of uncertainty about the endothelium geometry (σ_s) increases.

The mean flow velocity $\bar{u}$ and the standard deviation σ_{u_1} of the horizontal component of the flow velocity u_1 induced by randomly fluctuating pressure gradient $\nabla_{\boldsymbol{\xi}} p$ are shown in Figure 2.6. The flow is horizontal in the mean (Figure 2.6a). The no-slip boundary conditions at the walls imply that the horizontal component of flow velocity at the walls is known with certainty ($u_1 = 0$ at $\xi_2 = 0$ and $\xi_2 = 1$), so that $\sigma_{u_1} = 0$. Predictive uncertainty (σ_{u_1}) increases with the distance from the walls, reaching its maximum in the middle of the flow chamber, $\xi_2 = 0.5$.

Figure 2.7 reveals how the endothelium roughness (as quantified by σ_s and l_s) affects the mean flow velocity $\bar{u}$. The overall effect is to reduce the mean flow velocity relative to its counterpart resulting from the assumption of smooth endothelium ($\sigma_s = 0$). For a given σ_s, the mean velocity decreases as l_s becomes smaller, i.e., the endothelium surface becomes more irregular.

2.5.2 Flow rate and wall shear stress

The decrease in mean velocity with increasing endothelium roughness (Figure 2.7) translates into the corresponding decrease in the volumetric flow rate
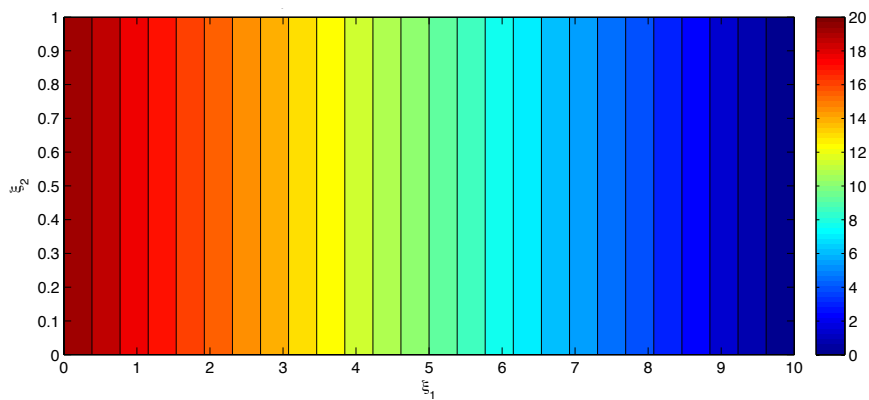
(a)
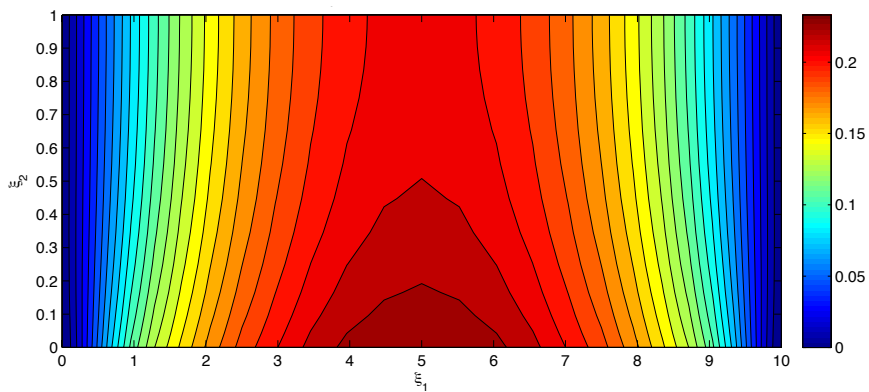
(b)

Figure 2.4: (a) Average pressure $\bar{p}$ and (b) deviations from the mean (standard deviation) σ_p.
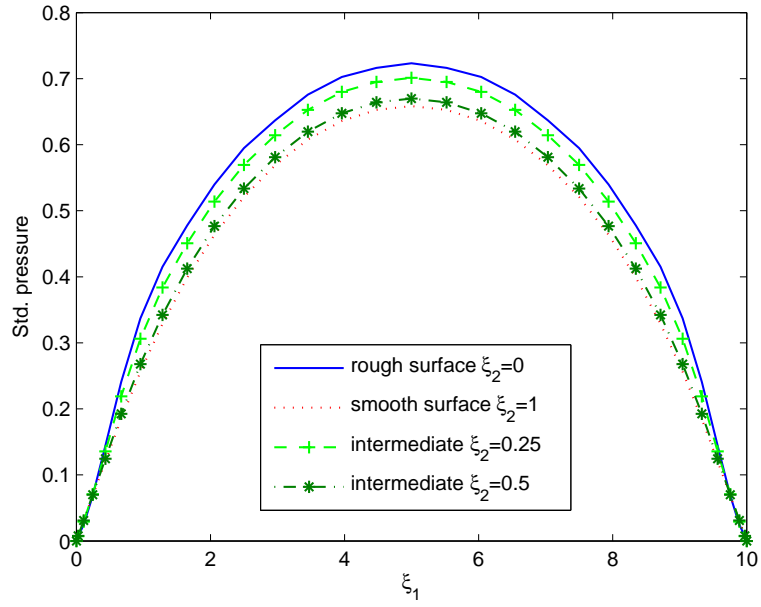
(a)
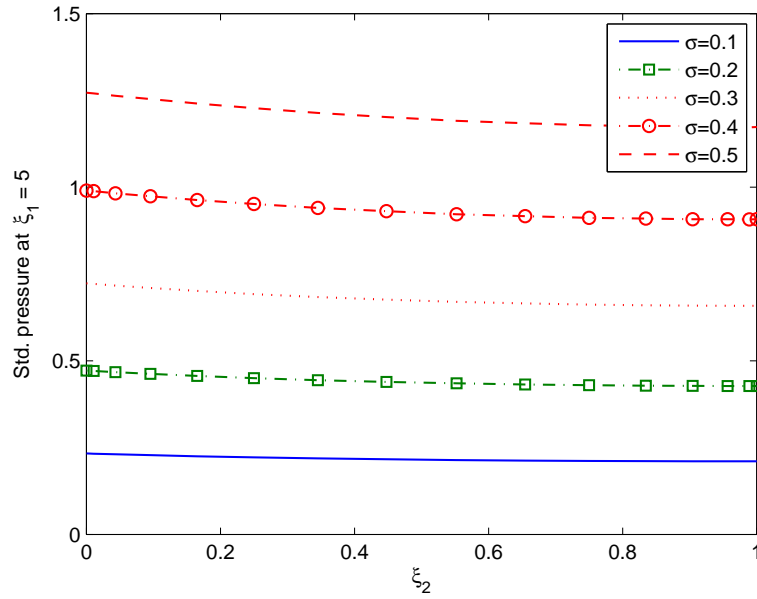
(b)

Figure 2.5: Standard deviation of pressure, σ_p, along several horizontal cross-sections $\xi_2 = c$ (a) and vertical cross-section $\xi_1 = L_x/2$ (b).
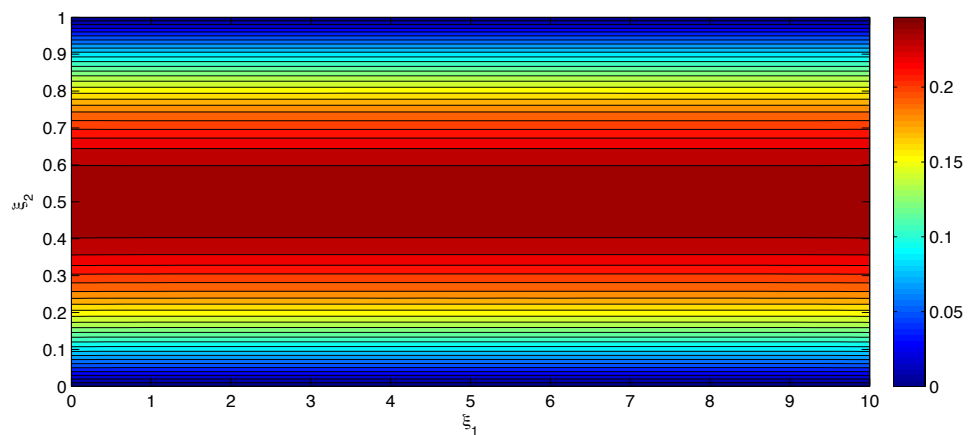
(a)
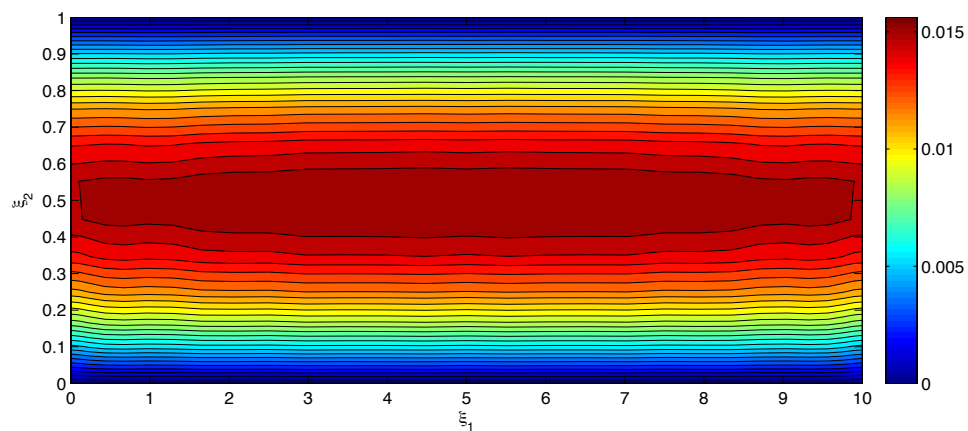
(b)

Figure 2.6: (a) Average flow velocity $\overline{u}$ and (b) deviations from the mean of the horizontal component of the flow velocity (its standard deviation) σ_{u_1}.
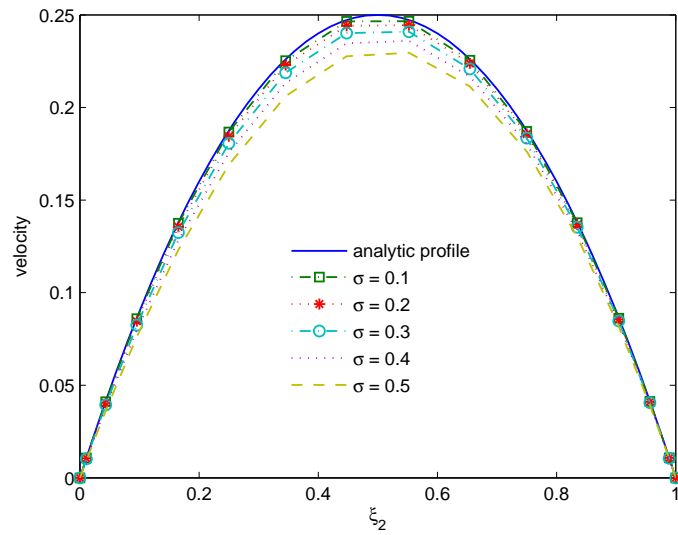
(a) $l_s = 1$
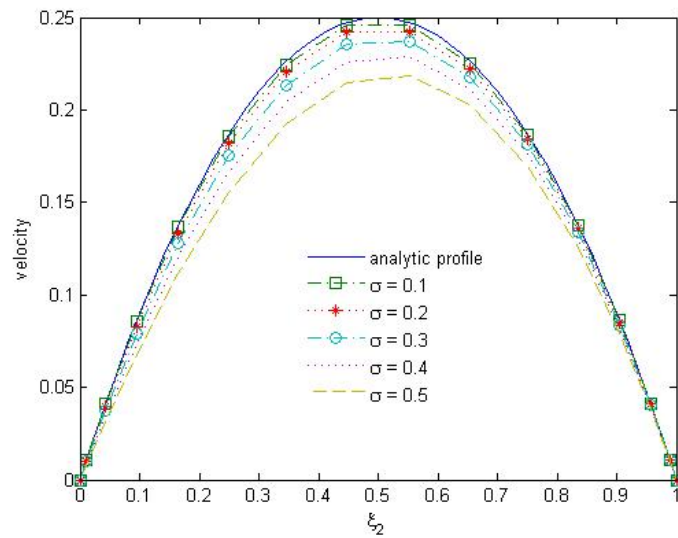
(b) $l_s = 0.7$

Figure 2.7: Mean velocity profiles $\overline{u}(L_x/2, \xi_2)$ for several degrees of endothelium roughness (σ_s and l_s).

$Q = \int_0^1 u_1 d\xi_2$. It is well known that, for a given pressure gradient, Q decreases as wall roughness increases. Figure 2.8 quantifies this effect in terms of the observable statistics of endothelium roughness, σ_s and l_s. The flow rate decreases as the roughness amplitude (standard deviation) σ_s increases and/or the correlation length l_s decreases.
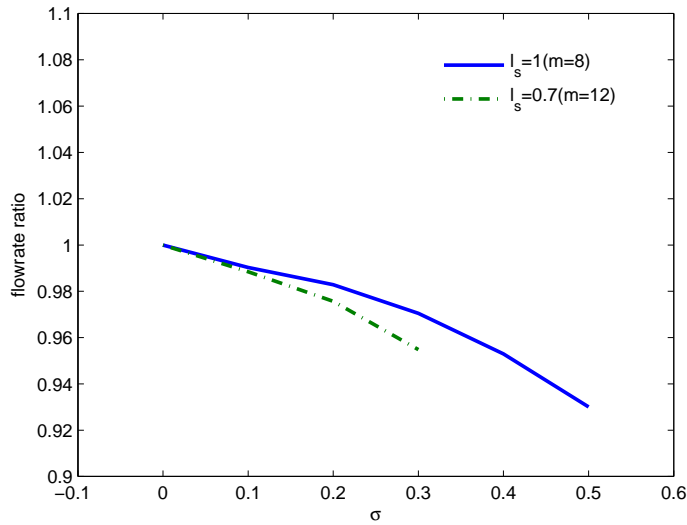
Figure 2.8: The volumetric flow rate, normalized with its counterpart in the flow chamber with smooth walls, as a function of the statistical parameters σ_s and l_s characterizing endothelium roughness.

Another quantity of physiological significance is the shear stress on the endothelium wall $s(x_1, \omega)$,

$$\tau_w(\xi_1, s; \omega) = \mu \frac{\partial u_1(\xi_1, s; \omega)}{\partial \xi_2}. \tag{2.27}$$

Spatial variability of the mean, $\overline{\tau}_w(\xi_1)$, and standard deviation, $\sigma_\tau(\xi_1)$, of

the endothelium shear stress τ_w is shown in Figure 2.9 for several degrees of endothelium roughness (σ_s and l_s). The mean shear stress $\overline{\tau}_w$ increases with both the magnitude of the endothelium fluctuations (its standard deviation σ_s) and its correlation length l_s. Predictive uncertainty (as quantified by σ_τ) increases with σ_s and, somewhat surprisingly, decreases with l_s. Boundary effects (deviation from the fully-developed flow regime, wherein the shear stress statistics are constant) extend further inside the flow chamber as σ_s increases and/or l_s decreases.

2.5.3   Effective blood viscosity

A classical treatment of blood flow in arteries whose walls are modeled as smooth surfaces relies on the Poiseuille law to relate the volumetric flow rate Q to the pressure gradient dp/dx,

$$Q = -\frac{L_y^3}{12\mu}\frac{dp}{dx}.$$

(2.28)

Accounting for (random) endothelium roughness requires one to replace the Poiseuille law in Eq. 2.28 with its "effective" or "equivalent" counterpart,

$$\overline{Q} = -\frac{L_y^3}{12\mu_e}\frac{d\overline{p}}{dx},$$

(2.29)

wherein μ_e denotes the effective viscosity.

Figure 2.10 demonstrates that μ_e, the blood viscosity inferred from in vivo experiments via the Poiseuille law, depends not only on blood properties but also on the statistical parameters characterizing the endothelium roughness (σ_s and l_s). The effective viscosity μ_e increases as σ_s increases and/or l_s decreases.
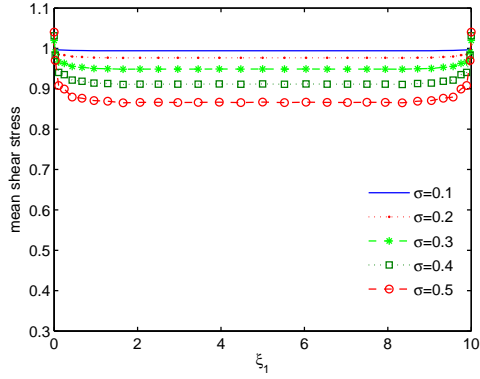
(a) $\overline{\tau}_w$ for $l_s = 1.0$

(b) $\overline{\tau}_w$ for $l_s = 0.7$

(c) σ_τ for $l_s = 1.0$
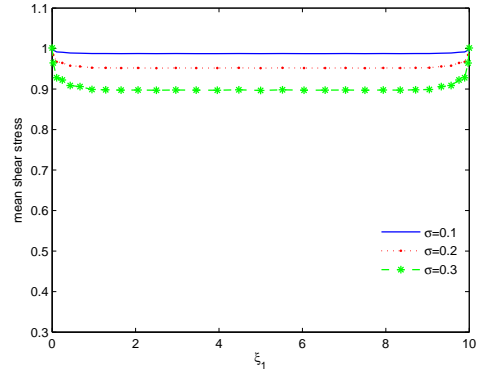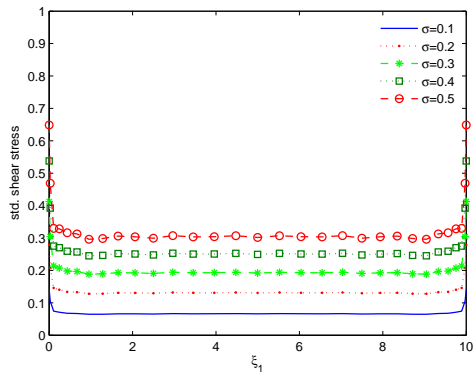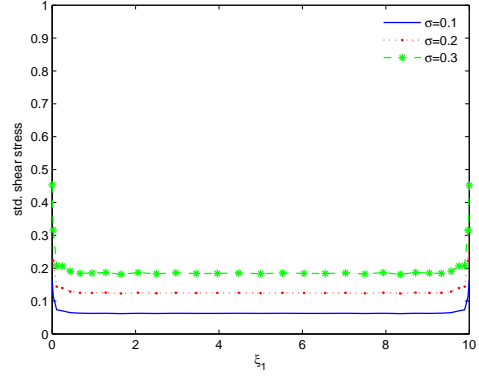
(d) σ_τ for $l_s = 0.7$

Figure 2.9: Spatial variability of the mean shear stress $\overline{\tau}_w(\xi_1, \xi_2)$ and its standard deviation $\sigma_\tau(\xi_1, \xi_2)$ along the endothelium wall $\xi_2 = 0$ for several degrees of endothelium roughness (σ_s and l_s).
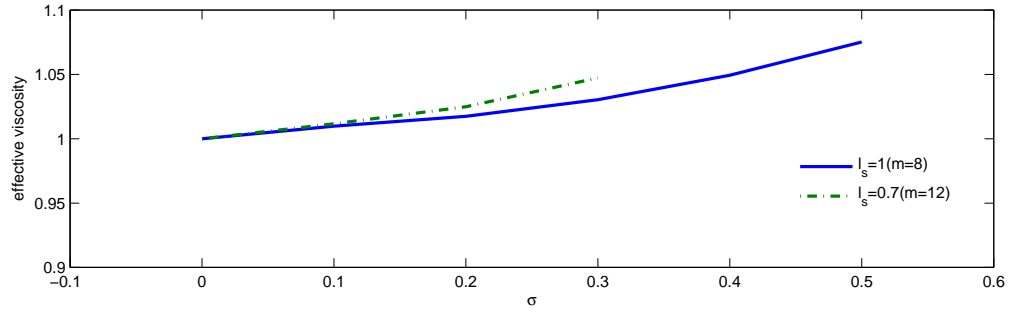
Figure 2.10: Effective blood viscosity μ_e, normalized with its counterpart corresponding to the smooth wall approximation, as a function of the endothelium roughness parameters σ_s and l_s.

2.6   Conclusions

We developed a computational framework to quantify the impact of uncertainty in the cell free layer (CFL) width on measured and observed flow characteristics (e.g., shear stress on endothelium walls). This is accomplished by treating the CFL surface as a random field with zero mean, standard deviation σ_s and correlation length l_s. This surface is represented via a Karhunen-Loève expansion. The Stokes equations defined on the resultant random domain are solved in two steps. First, the random flow domain is mapped onto a deterministic domain with smooth boundaries, which renders the transformed Stokes equations stochastic. Second, a generalized polynomial chaos expansion is used to solve these equations.

Our analysis leads to the following major conclusions.

- The mean pressure gradient is constant and unaffected by the endothelium

roughness. Uncertainty in (randomness of) the endothelium surface manifests itself in pressure fluctuations about the mean, as quantified by the standard deviation σ_p.

- The overall effect of endothelium roughness is to reduce the mean blood flow velocity relative to its counterpart corresponding to the assumption of smooth endothelium ($\sigma_s = 0$). For a given σ_s, the mean velocity decreases as l_s becomes smaller, i.e., the endothelium surface becomes more irregular.

- The decrease in mean velocity with increasing endothelium roughness translates into the corresponding decrease in the volumetric flow rate. The volumetric flow rate decreases as the roughness amplitude (standard deviation) σ_s increases and/or the correlation length l_s decreases.

- The mean shear stress increases with both the magnitude of the endothelium fluctuations (its standard deviation σ_s) and its correlation length l_s. Boundary effects (deviation from the fully-developed flow regime, wherein the shear stress statistics are constant) extend further inside the flow chamber as σ_s increases and/or l_s decreases.

- The blood viscosity, inferred from in vivo experiments via the Poiseuille law, depends not only on blood properties but also on the statistical parameters characterizing the endothelium roughness (σ_s and l_s). The effective blood viscosity increases as σ_s increases and/or l_s decreases.

S.-W. Park, M. Intaglietta and D. M. Tartakovsky, "Impact of endothelium roughness on blood flow", J. Theor. Biol., vol. 300, doi:10.1016/j.jtbi.2012.01.017, pp. 152-160, 2012.

Chapter 3

Alternative Representation of

Random Surfaces

Consider the stochastic process in a finite interval $T = [-L, L]$ of a one-dimensional space. A Fourier series provides a natural representation of such random fields, and can be viewed as a special case of the KL expansions [47, 21, 48, 49, 50]. Thus, a random field $v(x, \omega)$ can be represented by a Fourier-like series

$$v(x) = \frac{a_0}{\sqrt{2}}\xi_0 + \sum_{n=1}^{\infty}\left[\left(a_n \cos \frac{2n\pi}{T}x\right)\xi_n + \left(b_n \cos \frac{2n\pi}{T}x\right)\eta_n\right] \qquad (3.1)$$

where ξ_n and η_n are independent identically-distributed random variables. The covariance function $C_v(x_1, x_2) = \langle v(x_1)v(x_2)\rangle$ is defined as

$$C_v = \frac{a_0^2}{2} + \sum_{n=1}^{\infty}\left[\frac{a_n^2 + b_n^2}{2}\cos \frac{2n\pi}{T}(x_1 - x_2) + \frac{a_n^2 - b_n^2}{2}\cos \frac{2n\pi}{T}(x_1 + x_2)\right]. \qquad (3.2)$$

A (bilateral) second-order autoregressive process with a periodic condition is related to a solution of the modified Helmholtz equation [47, 21]. Specifically, for

the period $T = 2L$ and $v(0) = v(L) = 0$, the covariance is given explicitly by

$$C_v = \sum_{n=1}^{\infty} \frac{b_n^2}{2} \left[\cos \frac{n\pi}{L}(x_1 - x_2) - \cos \frac{n\pi}{L}(x_1 + x_2) \right], \qquad b_n^2 = \frac{2}{Lk^4} \left[1 + \left(\frac{n\pi}{Lk} \right)^2 \right]^{-2}$$

(3.3a)

This random process is represented by a sine Fourier expansion,

$$v(x) = \sum_{n=1}^{\infty} \eta_n b_n \sin \frac{2n\pi}{T} x.$$

(3.4)

This expansion is described in detail in [47, 21, 50]. We adopt this representation in order to solve the Stokes equations in random domains.

3.1 Problem formulation

Consider Stokes flow between two parallel plates, one of which is randomly rough. The random flow domain is $\mathcal{D} : \{(x, y) \in [-T/2, T/2] \times [h, \delta]$. The upper plate, $y = \delta$, is smooth and deterministic. The lower plate, $y = h$, is a random surface represented by the truncated expansion with zero mean ($\bar{h} = 0$),

$$h(x; \omega) = \bar{h}(x) + \sigma \sum_{k=1}^{N} b_k \sin \left(\frac{2k\pi x}{T} \right) \xi_k(\omega),$$

(3.5)

in which the random variables $\xi_k(\omega)$ are uniformly distributed, T is the length of the process along the x-axis, σ controls the strength of the process, and

$$b_k = \frac{2}{\sqrt{T}\ell^2} \left[1 + \left(\frac{2\pi n}{T\ell} \right)^2 \right]^{-1},$$

(3.6)

where $\ell = T/\ell_s$ and ℓ_s is the correlation length of $h(x; \omega)$. The random variables $\xi_k(\omega)$ have zero mean and unit variance on $\xi_k(\omega) \in [-\sqrt{3}, \sqrt{3}]$.

To compute the periodic problem, we adopt the covariance kernel intro-
duced in [47, 21]. We solve the periodic Stokes flow problem with $\delta = 1$, $\sigma = 0.2$
or 0.4, and $\ell = T/l_s = 2$. This choice of the correlation length ratio ℓ facilitates
representation of the roughness in a higher-dimensional random space at a man-
ageable cost. This means that more stochastic dimensions are needed at higher
accuracy as the correlation length decreases. The number of terms in the Fourier
expansion that are necessary to represent $h(x; \omega)$ with a given degree of accuracy
(α) are presented in Table 3.1. Typical realizations of the random plate $h(x; \omega)$,
for the above-mentioned statistical parameters and the Fourier expansion with the
accuracy $\alpha = 95\%$, are shown in Fig. 3.1. We computed the problem with two
cases of $\alpha = 95\%$

Table 3.1: The truncated number of terms in the KL expansion (3.5), obtained by
using $\Sigma_{n=1}^{N}(b_n^2) \geq \alpha\Sigma_{n=1}^{\infty}(b_n^2)$ criterion at the correaltion length ratio $\ell = 2.0$.

α	$N(l_s = 1, T = 2)$	$N(l_s = 5, T = 10)$
90%	2	5
95%	2	6
99%	4	12

Figure 3.2 demonstrates that the smaller the correlation length, the more
random/rough the surface. A deterministic domain on which the transformed
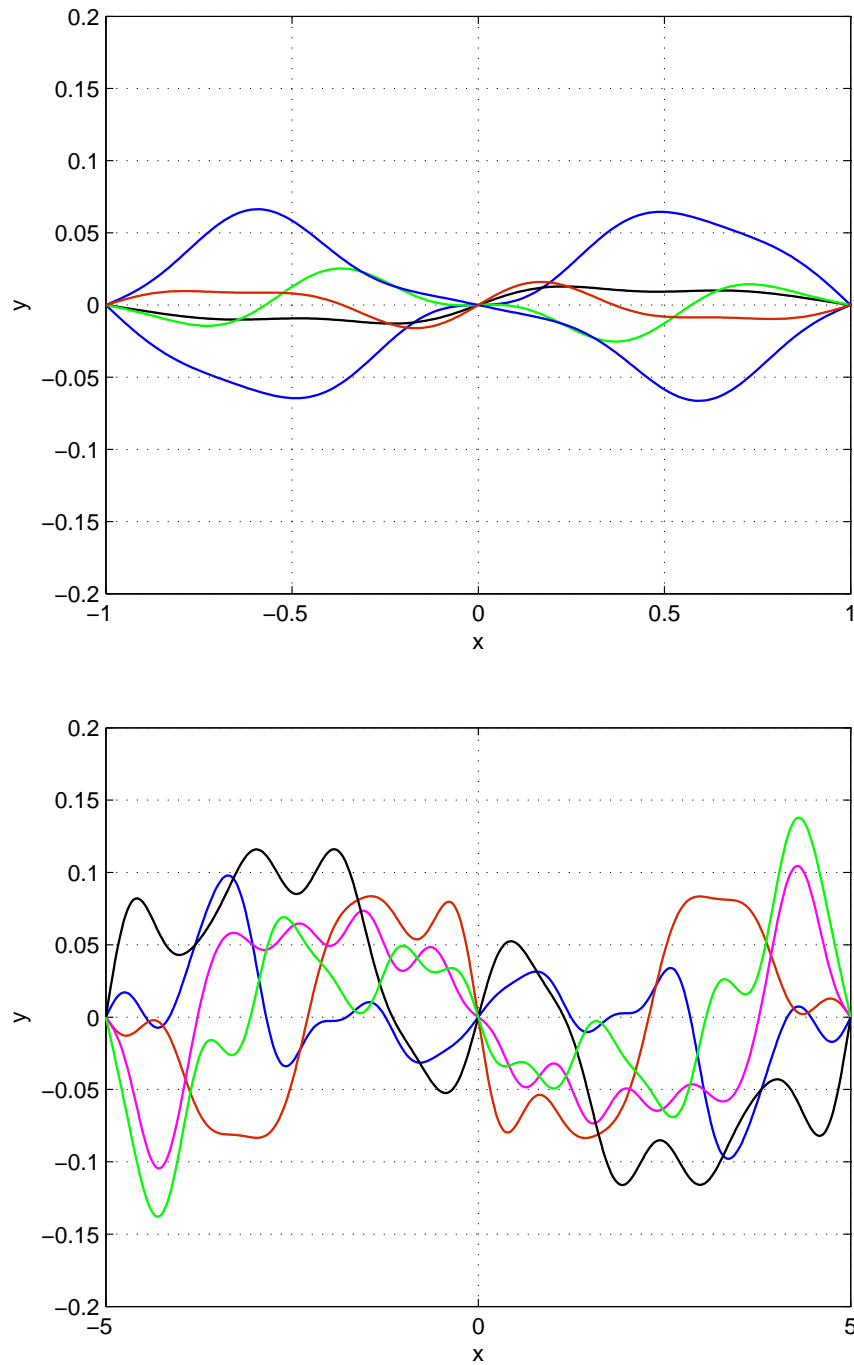
Figure 3.1: Realizations of the random bottom plate of the channel for $\ell = 2.0$ and the channel length $T = 2$ ($\ell_s = 1$ upper) and 10 (below).

stochastic equations are to be solved is $D : \{(x, y) \in [-T/2, T/2] \times [0, 1]$.

The flow is driven by the externally applied pressure gradient $-\partial P/\partial x = 2$.
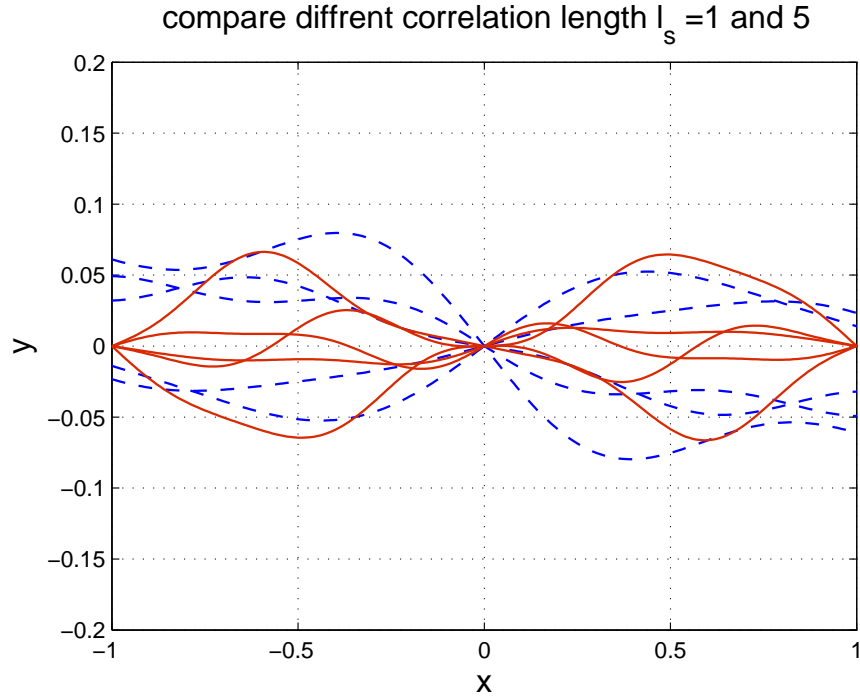
Figure 3.2: Realizations of the random bottom plate of the channel for $\ell = 2.0$ and the channel length $T = 2$ ($\ell_s = 1$ red) and 10 ($\ell_s = 5$ blue) in the same region ($-1 < x < 1$).

3.2   Results and Discussion

We use the mapping approach [51, 23] to compute this periodic Stokes flow problem. This is a two-step computational method: first, a random flow domain is mapped onto a deterministic domain; second the transformed stochastic

counterparts of Stokes equations are solved in a deterministic domain using a stochastic Galerkin method (SGM) with generalized polynomial chaos expansions (gPC) in the probability space and a spectral element method in the physical space. This approach is briefly outlined in Appendix A. In the mapping approach, an extensive effort has been made to obtain the grid-independent (converged) first and second moments of the horizontal (u) and vertical (v) components of the random velocity vector.

The stochastic mapping function is defined by $\eta_1 = x$ and $\eta_2 = (y - h)/(1 - h)$. It transforms the random flow domain $\mathcal{D}^f$ into a deterministic domain $D^t : \{(\eta_1, \eta_2) \in [-T/2, T/2] \times [0, 1]$. The ensemble statistics of $u(x, \eta_2; \omega)$ are displayed at a few cross-sections $x = $ const. Based on the covariance kernel and the correlation length utilized, we chose the cross-sections $x = \pm 0.5$ for $T = 2$ and $l_s = 1$, and the cross-sections $x = \pm 2.5$ for $T = 10$ and $l_s = 5$. In both cases, these cross-sections correspond to the locations with the maximum variance of the random roughness $h(x, \omega)$.

Figure 3.3 exhibits the mean velocity profiles across the channel width, $\mathbb{E}[u]$, for $l_s = 1$ and either $\sigma = 0.2$ or $\sigma = 0.4$. As expected, Fig. 3.3 demonstrates that the mean centerline velocity and, hence, the volumetric flow rate decrease as the wall roughness (σ) increases.

Figure 3.4 shows the standard deviation of $u(x, \eta_2; \omega)$ computed at $x = \pm 0.5$. Since the wall roughness is highest at $x = \pm 0.5$, one can expect the maximum predictive uncertainty (as quantified by $Std[u]$) to occur at these cross-sections.
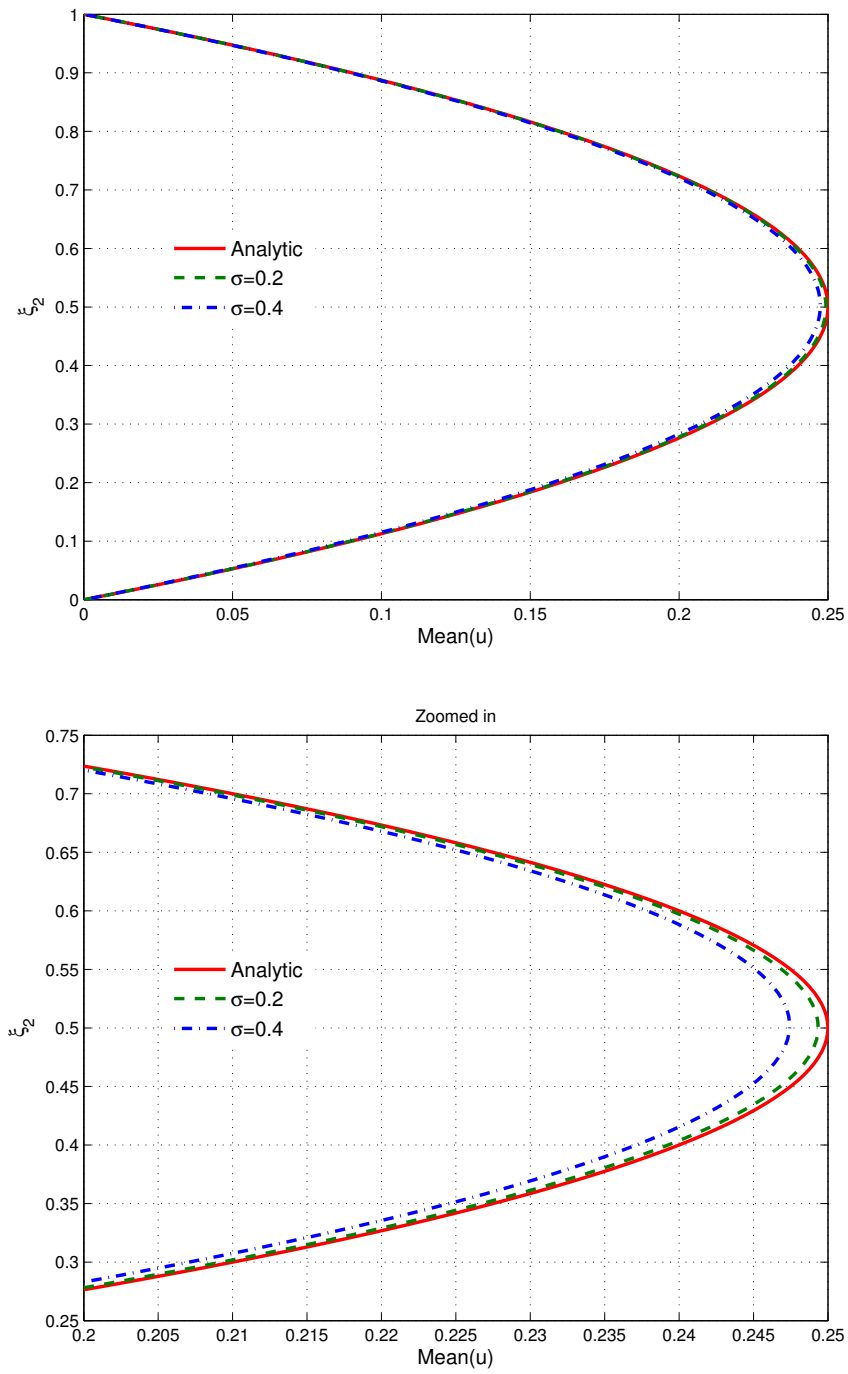
Figure 3.3: Mean velocity profiles across the channel width for $l_s = 1$ and either $\sigma = 0.2$ and $\sigma = 0.4$. Also shown are the Poiseuille velocity profiles (Analytic) for smooth walls.

Figure 3.4 reveals that vertical profiles of $Std[u]$ at $x = 0.5$ and $x = -0.5$ are the same and distinct from the profiles at $x = 0$ in which the roughness is lowest. The maximum value of $Std[u]$ is towards the random wall ($\eta_2 \approx 0.25$) in both cases ($\sigma = 0.2$ or 0.4). The location of highest predictive uncertainty is seen to be insensitive to the strength of wall randomness ($\sigma = 0.2$ or 0.4).
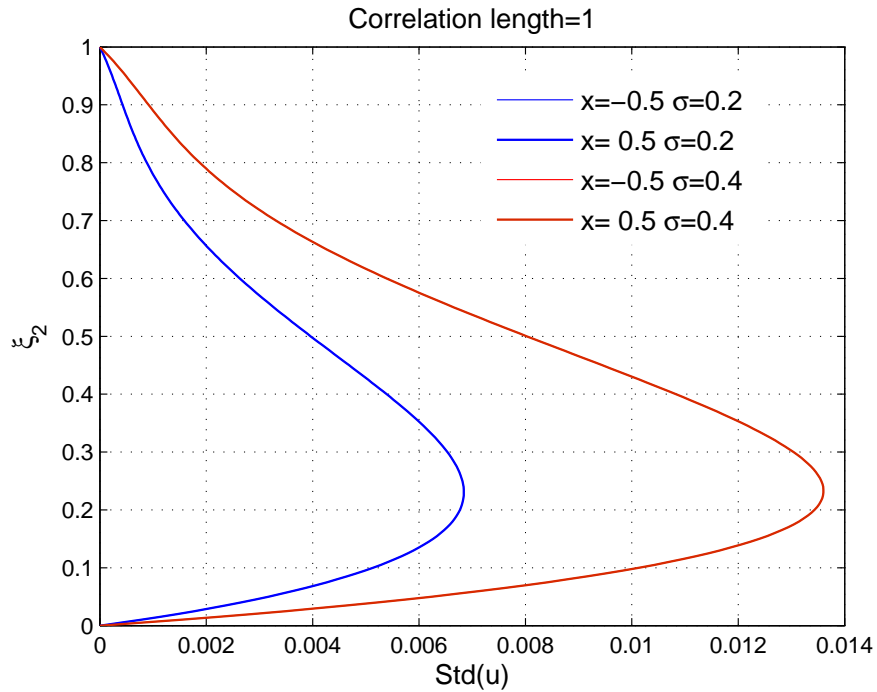
Figure 3.4: Standard deviation of u at $x = \pm 0.5$ for $l_s = 1$ and $\sigma = 0.4$ and $\sigma = 0.2$.

The process by which the random wall roughness has been generated results in the known (deterministic) position of the bottom wall $h = 0$ at $x = 0$ (Fig. 3.1). Therefore, it is reasonable to expect that the predictive uncertainty, i.e., $Std[u]$ and $Std[v]$, is smallest at $x = 0.0$. Yet it is not zero due to random fluctuations of

the rough wall in the neighborhood of $x = 0.0$. Figure 3.5 demonstrates that this is indeed the case. The standard deviation of u at $x = 0.0$ is almost an order of magnitude smaller than its counterpart at $x = 0.5$ (Fig. 3.4).

The presence of random roughness induces the vertical fluctuations in flow velocity. While $\mathbb{E}[v] = 0$, the standard deviation of the vertical velocity component $Std[v]$ is appreciable (Fig.3.5). In fact, at $x = 0.0$ it is an order of magnitude higher than $Std(u)$. Figure 3.6 shows that the peak positions of $Std(u)$ and $Std(v)$ are insensitive to the strength of the random roughness σ.

The comparison of Figs. 3.3 and 3.7 demonstrates that the flow rate decreases as l_s increases. The impact of larger correlation lengths ($l_s = 5$) on the standard deviation of u and v is found in Figs. 3.5 and 3.6. The comparison of these figures demonstrates that the location of maximum fluctuations moves closer toward the random rough wall as ℓ_s decreases, i.e., the wall becomes rougher (Fig. 3.2).

Figure 3.8 shows that the number of grid points in the x direction affects predictions of the flow behaviors since the representation of roughness is based on the limit of a second-order autoregressive process with a periodic condition [21]. That process is derived from a modified Helmholtz equation with the limit of $\Delta x \to 0$ and is dependent upon the length between grid points.
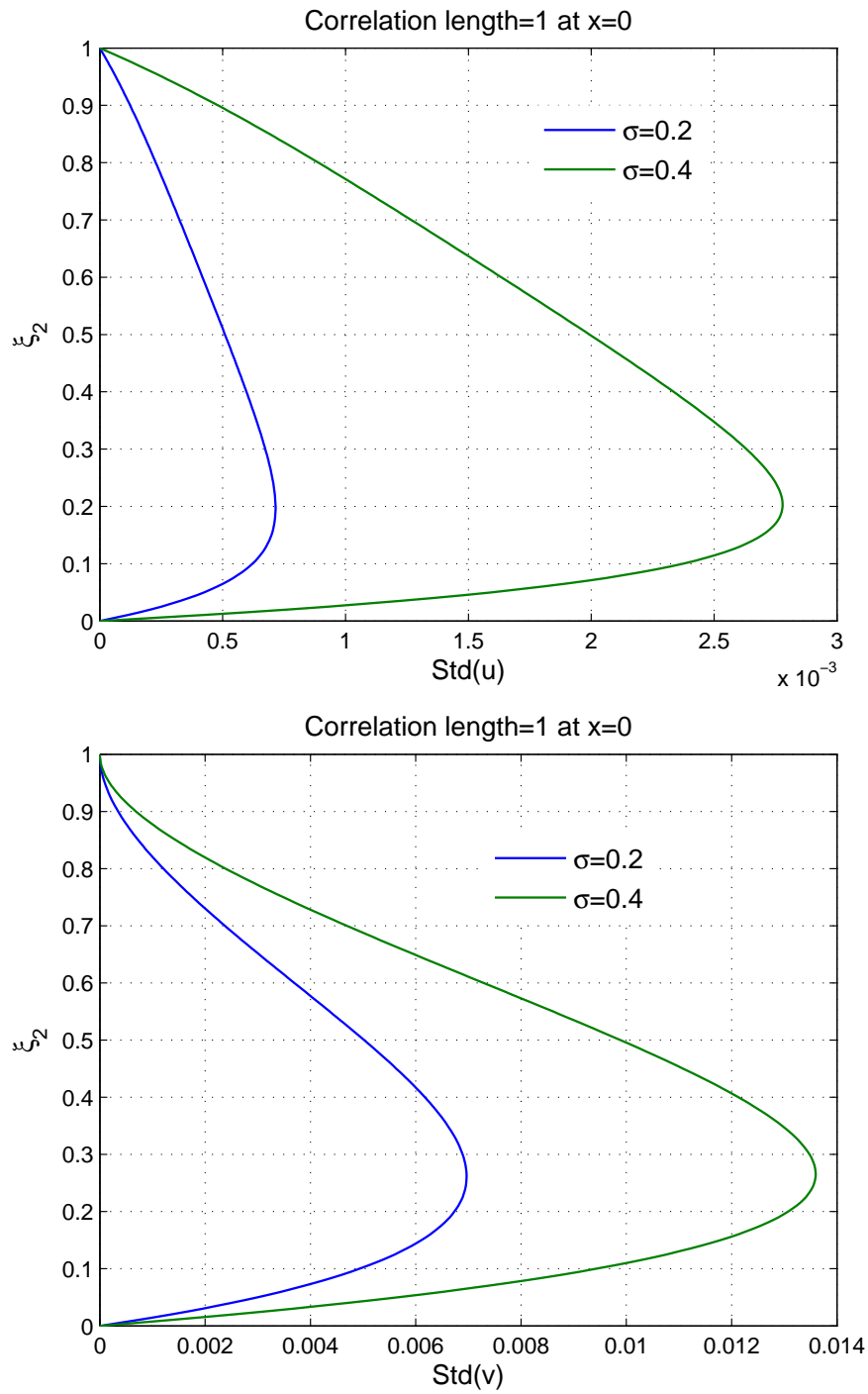
Figure 3.5: Standard deviations of u (upper) and v (lower) at $x = 0.0$ for $l_s = 1$ and $\sigma = 0.4$.
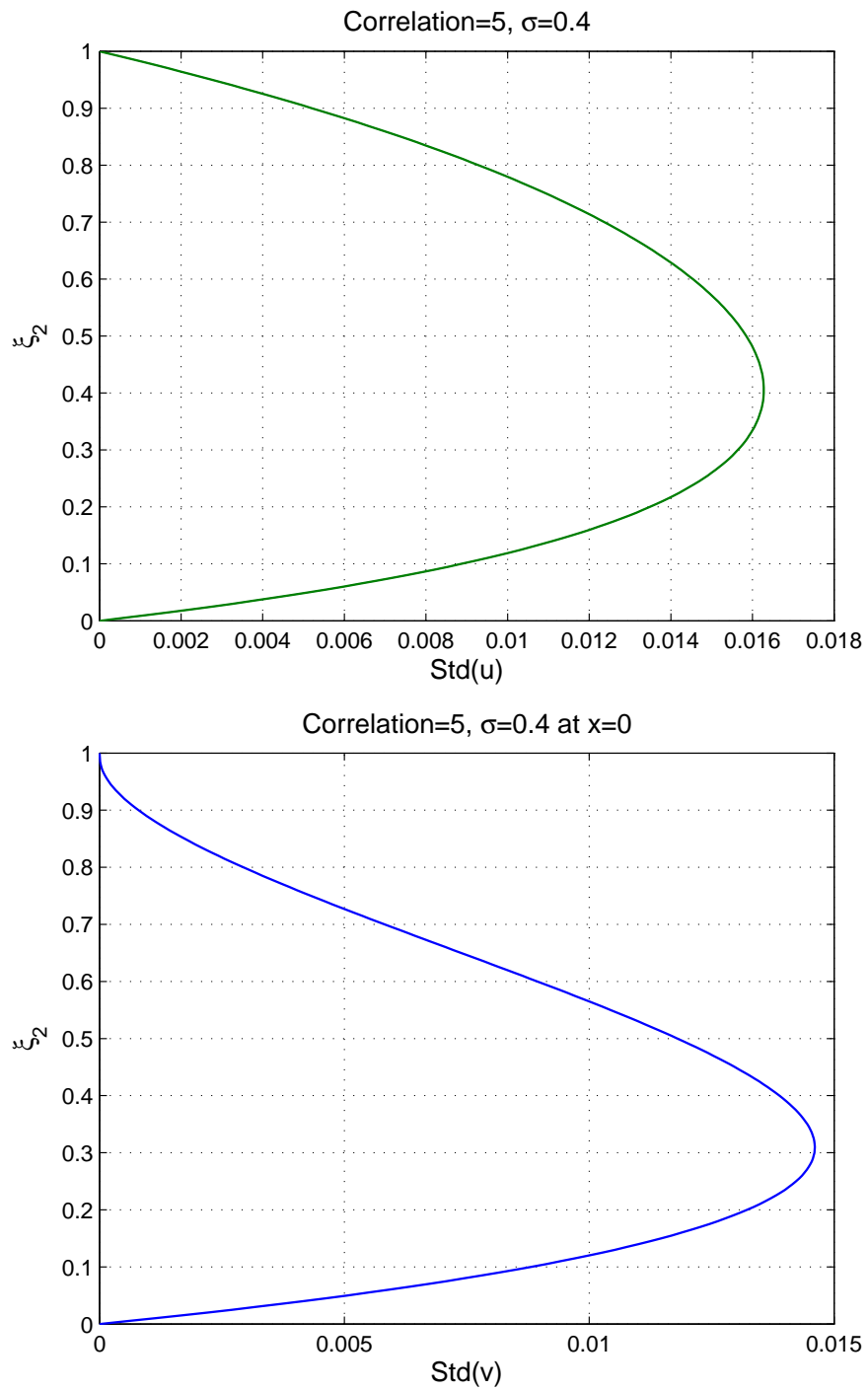
Figure 3.6: Standard deviations of u at $x = \pm 2.5$ (upper) and v at $x = 0.0$ (lower) for $l_s = 5.0$ and $\sigma = 0.4$.
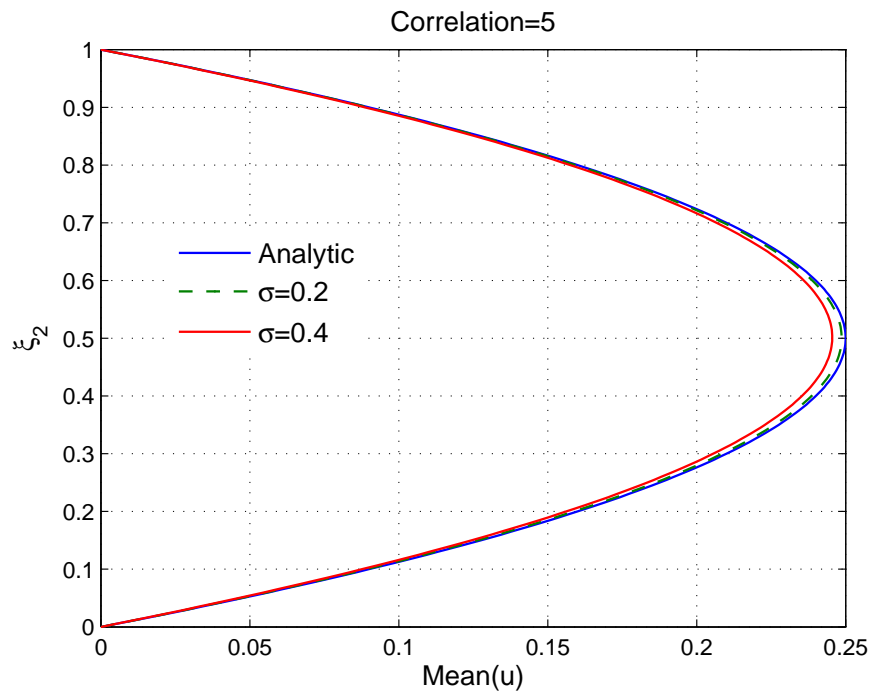
Figure 3.7: Mean velocity profiles across the channel width computed at $x = 0.5$ for $l_s = 5.0$ and $\sigma = 0.4$. Also shown is the Poiseuille velocity profile (Analytic) for smooth walls.
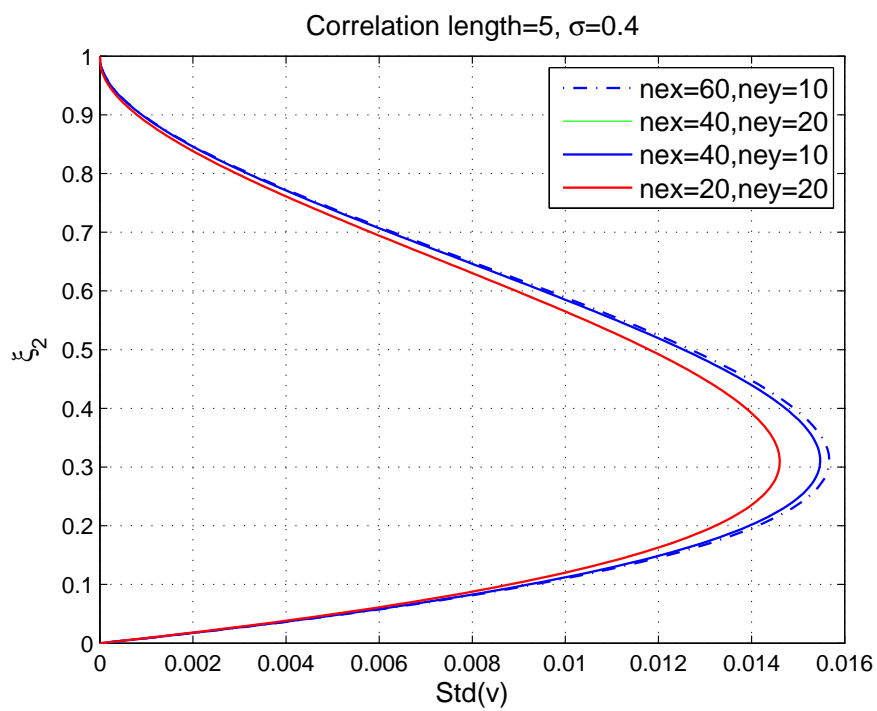
Figure 3.8: Standard deviations of v at $x = 0.0$ for $l_s = 5.0$ and $\sigma = 0.4$ in the case of different grid points

3.3   Summary and conclusions

We analyzed Stokes flow with periodic conditions in a random domain by using the stochastic mapping approach and stochastic Galerkin method, which is an intrusive approach that leads to a set of M deterministic coupled PDEs. The finite number of stochastic expansion is computed as $M = \frac{(N+P)!}{N!P!}$, where P is the order of polynomials in the gPC expansions. Since it is difficult to solve the problem with periodic conditions by using the Karhunen-Loéve expansion described in Chapter 2, the random roughness was modeled by a second-order autoregressive process and was represented using another form of Karhunen-Loéve expansion for the periodic flow.

Our study leads to the following major conclusions:

- Random roughness reduces the volumetric flow rate and increases the magnitude of fluctuations of the velocity components; this reduction becomes more pronounces as the roughness' variance increases and/or its correlation length decreases.

- The peak of predictive uncertainty is shifted from the channels centerline towards its random wall. The location of maximum predictive uncertainty is insensitive to the roughness' variance but is affected by its correlation length. The location of maximum fluctuations moves toward the random surface with smaller correlation length (the surface becomes rougher).

Chapter 4

Reaction-Diffusion in Random Domains

4.1 Introduction

Nitric oxide (NO) plays a critical role in the control of smooth muscle tone, ultimately regulating blood flow at the microvascular level. The distribution of NO in the microcirculation is determined by the balance between NO production and consumption in the blood and tissue compartments. The local concentration of NO in blood results from the competition between NO diffusing from the endothelium and NO scavenging by hemoglobin contained by red blood cells (RBCs) (or at times dissolved in plasma). Mathematical modeling of this process has been used [52, 53, 54, 55, 32, 37, 56, 57] to determine the NO distribution in cylindrical and parallel-plate compartments that simulate blood vessels as a function of local transport

parameters, such as NO production rate, scavenging reaction rate and diffusion coefficients in blood and tissue.

A significant portion of the NO involved in the regulation of blood flow is generated by mechanotrasduction [32, 57] via shear stress developed by flow at the vascular (WSS). This is the mechanical effector that links the biochemistry of NO production by the endothelium with flow conditions since the effects of NO on vessel diameter determine the anatomical component of vascular flow resistance. Shear stress is developed at the vascular wall by tangential stresses caused by flowing blood whose RBC concentration (hematocrit, Hct) diminishes from maximal at the blood flow core to zero in the cell free layer (CFL) next the vessel wall. Therefore the fluid next to the vessel wall can be modeled as a two layer system by assuming two immiscible fluids. Flow velocity profiles can be assumed to be parabolic within the CFL and plug-like in the RBC core region [37, 58, 59]. Flow in the latter region exhibits non-Newtonian behavior.

Changes of NO production due to changes in WSS caused by the variation of blood flow and plasma viscosity [60] appear to dominate other factors, such as changes in hemoglobin concentration or Hct [55, 32, 37, 56, 61]. Experimental evidence (e.g., [62]) suggests that NO production rate by the endothelium varies linearly with WSS (see also [53, 63]). However there appears to be a fundamental difference in the rate of production between steady and time-varying WSS [53], the latter being significantly greater. It should be noted that this effect is found for macroscopic time-varying flow (and therefore shear stress) imposed on endothe-

lialized surfaces obtained by cell culture techniques.

The virtually universal method of studying endothelial shear stress responses in parallel plate flow chambers, where endothelial cells are grown to a confluent layer on the plates, has significantly advanced our understanding of their reactions to different flow and shear stress regimes. However it is recognized that the experimental set up differs from in vivo conditions in some potentially important ways, such as using culture media fluid instead of blood and the use of high oxygen tension.

Another hitherto not considered, yet potentially significant, difference between the experiments and reality stems from microscopic spatio-temporal fluctuations of the CFL width. These fluctuations are due to both the microscopic spatial variability of the endothelial surface (blood vessel walls) [64, 65] and the stochastic, time-dependent variability of the outer layer of RBCs in the flowing blood column. The latter is caused by the shear-rate-gradient-induced torque on RBCs and the physical interactions between cells. Consequently, RBCs' deformations and aggregation produce a highly irregular surface between the blood column and the CFL [66, 67], affecting flow and shear stress on the endothelium. These unpredictable fluctuations can be captured by treating the CFL width at any given location as a random field that determines the distance between the NO source and its sink. Another mechanism by which the stochasticity of the CFL width affects NO concentration is due to its repercussion on the local, microscopic variability of the flow field, and therefore on shear rates and shear stresses.

While the (random) spatio-temporal fluctuations of CFL width and its bounding surfaces clearly affects NO bioavailability and production rate, most studies (including those mentioned above) treat the interface between the RBC column and plasma as a smooth deterministic surface. In the present study, we adopt a more realistic approach by treating the surface flowing RBCs and the CFL as a random field whose statistics are calculated from the experimental studies [53, 2]. Within this conceptual framework, we formulate a model that describes the NO bioavailability in microcirculation. More specifically, our objective is to determine the distribution of NO concentration in the regions of the interface between blood and tissue at the blood vessel wall (RBC-rich core, cell free layer, and tissue layer) [52].

4.2 Mathematical Model of NO Transport

4.2.1 Model Formulation

According to the standard Krogh tissue cylinder model, an arteriolar cross-section consists of the RBC-rich core ($E^1 : 0 \leq r \leq r_1$), the CFL ($E^2 : r_1 < r \leq r_2$), the endothelial-cell region ($E^3 : r_2 < r \leq r_3$), and the smooth-muscle region ($E^4 : r_3 < r \leq r_4$). Stochastic fluctuations of the interface formed by flowing RBCs, $r_1(\theta, t)$, are modeled by treating it as a random function of both angular coordinate θ and time t, i.e., $r_1 = r_1(\theta, t; \omega)$ with $\omega \in \Omega$ indicating a realization ("coordinate") in the probability space Ω. This renders the CFL width $w = r_2 - r_1$ random, i.e.,

$w = w(\theta, t; \omega)$. Our goal is to capture the effects of stochastic fluctuations of the RBC-CFL interface $r_1(\theta, t; \omega)$ on distribution of NO concentration, C_{NO}, in the Krogh tissue cylinder $\mathcal{D} = \{(r, \theta) : 0 \leq r \leq r_4, 0 \leq \theta \leq 2\pi\}$.
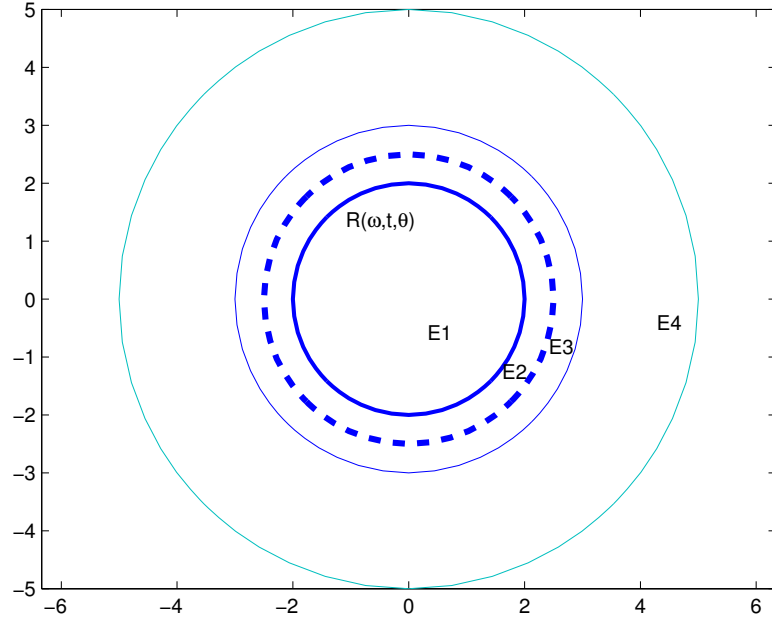
Figure 4.1: Arteriolar cross-section is conceptualized by the Krogh tissue cylinder model (not to scale, $R = r_1$).

In each region of the computational domain, E^i $(i = 1, \ldots, 4)$ (Fig. 4.1), the concentration C_{NO} satisfies a reaction-diffusion equation

$$\frac{\partial C_{\mathrm{NO}}}{\partial t} = D_i \nabla^2 C_{\mathrm{NO}} - k_i C_{\mathrm{NO}}, \qquad (r, \theta) \in E^i, \tag{4.1}$$

where D_i and k_i are the diffusion coefficient and degradation (reaction) rate in the i-th region, respectively. These four equations are coupled by the continuity

conditions at the interfaces r_i $(i = 1\ldots, 3)$,

$$C_{\mathrm{NO}}^- = C_{\mathrm{NO}}^+, \qquad F_n^- - F_n^+ = \dot{q}_i, \qquad r = r_i. \tag{4.2}$$

Here the superscripts $^-$ and $^+$ indicate the left and right limits of the corresponding quantities at the i-th interface, $F_n = \mathbf{F}_i \cdot \mathbf{n}_i$ is the normal component of Fick's flux $\mathbf{F}_i = -D_i \nabla C_{\mathrm{NO}}$ at the i-th interface whose outward unit normal is $\mathbf{n}_i$, and $\dot{q}_i$ denotes the NO production rates at the interface $r = r_i$. Since only endothelium cells are involved in NO production, $\dot{q}_1 \equiv 0$. We assume that no nitric oxide leaves the outer boundary of the smooth-muscle region, $r = r_4$, so that

$$\mathbf{n} \cdot \nabla C = 0, \qquad r = r_4. \tag{4.3}$$

The coupling of the reaction-diffusion equations (4.1) at the interfaces $r = r_i$ $(i = 1, 2, 3)$ propagates uncertainty (randomness) in the topology of the RBC-CFL interface $r_1(\theta, t; \omega)$ through the modeling process, leading to randomly varying NO concentration $C_{\mathrm{NO}}(r, \theta, t; \omega)$ throughout the Krogh tissue cylinder.

4.2.2 Model Parameterization

While the reaction rates k_i in the endothelium $(i = 3)$ and tissue $(i = 4)$ can be considered constant [54, 68, 56], the reaction rate in the RBC-rich core (k_1) is related to hemoglobin levels. The latter depends on hematocrit $H(r)$ and radial component of blood flow velocity $V(r, \theta, t)$. Let k_s denote the reference rate of NO scavenging by RBCs at the reference level of hematocrit H_s. Then, the NO

scavenging rate k_1 corresponding to a given hematocrit level H_c is given by [53, 32]

$$k_1 = \frac{H_c}{H_s}k_s.\qquad(4.4)$$

The hematocrit ratio H_c/H_s is determined by mass conservation,

$$\int_0^{2\pi}\int_0^{r_2} H(r,t)V(r,\theta,t)r\mathrm{d}r\mathrm{d}\theta = H_s\int_0^{2\pi}\int_0^{r_2} V(r,\theta,t)r\mathrm{d}r\mathrm{d}\theta.\qquad(4.5)$$

In the general stochastic framework we advocate here, blood is a two-phase fluid that exhibits non-Newtonian behavior in the RBC-rich core and Newtonian one in the CFL, with the random surface $r_1(\theta,t;\omega)$ separating the two regions. This implies that flow velocity $V(r,\theta,t;\omega)$ is random as well, being given by a solution of corresponding flow equations in random domains [51]. To focus on NO transport, we simplify the flow calculations by adopting two alternative approximations.

The first is based on a lubrication approximation in which random geometry parameterizes an otherwise deterministic velocity profile [69]. This approach yields a random velocity profile $V(r,\theta,t;\omega)$,

$$\frac{V}{V_{\max}} = \begin{cases} 1 - \dfrac{\mu_p}{\mu_c}\dfrac{r^2}{r_2^2} - \left(1 - \dfrac{\mu_p}{\mu_c}\right)\dfrac{r_1^2}{r_2^2} & 0 \le r \le r_1 \\[2ex] 1 - \dfrac{r^2}{r_2^2} & r_1 \le r \le r_2 \end{cases}\qquad(4.6)$$

where $V_{\max} = Jr_2^2/(4\mu_p)$ is the (maximal) centerline velocity, J is the externally imposed pressure gradient, and μ_p and μ_c are the viscosities of the plasma viscosity and RBC-rich core. In this formulation, the only source of the non-Newtonian behavior of the RBC-rich core is the dependence of the core viscosity μ_c on the (random) CFL width. Following [58] and many others, we assume a linear relationship

$\mu_c = 0.1678H_c - 4.348$ between a hematocrit level H_c and the viscosity of the RBC core μ_c. Specifying a (random) radial distribution of hematocrit, $H = H(r, t; \omega)$, as a step function

$$\frac{H}{H_c} = \begin{cases} 1 & 0 \leq r \leq r_1 \\ \\ 0 & r_1 < r \leq r_2 \end{cases} \tag{4.7}$$

enables one to compute the randomly fluctuating NO scavenging rate $k_1(t; \omega)$ by combining (4.4)–(4.7). First, the system of equations (4.5)–(4.7) was solved using Matlab function "Solve" to compute H_c for $\mu_p = 1.2$ cP and two values of H_s. Then $k_1(t; \omega)$ was obtained from (4.4).

The second alternative for obtaining $k_1(t; \omega)$ treats the blood as a single-phase fluid with a parabolic velocity profile

$$\frac{V}{V_{\max}} = 1 - \frac{r^2}{r_2^2}, \qquad 0 \leq r \leq r_2. \tag{4.8}$$

The CFL and the random RBC-CFL interface $r_1(\theta, t; \omega)$ enter this formulation via a radial distribution of hematocrit,

$$\frac{H}{H_c} = \begin{cases} 1 & 0 \leq r \leq r_1 \\ \\ \left(\dfrac{r_2 - r}{r_2 - r_1}\right)^2 & r_1 \leq r \leq r_2 \end{cases} . \tag{4.9}$$

Combining (4.4)–(4.7) yields an alternative expression for the NO scavenging rate $k_1(t; \omega)$. This approach was used in [54, 68, 56] in the deterministic context that treated $r_1(\theta, t)$ as constant.

Finally, we allow the NO production rates by the endothelium, i.e., $\dot{q}_2$ and $\dot{q}_3$ in (4.2), to vary with the wall shear stress τ_w exerted on the endothelium walls

by blood flow. Following [2, 53, 52], we assume a linear relation

$$\dot{q}_2 = \dot{q}_3 = \frac{\tau_w}{\tau_w^\star}\dot{q}^\star, \qquad \tau_w = \mu_p \frac{V_{edge}}{w}, \tag{4.10}$$

where $\tau^\star$ is the reference wall shear stress, $\dot{q}^\star$ is the control NO production rate, and V_{edge} is the mean velocity at the outer edge of RBC cores. These production rates fluctuate randomly, i.e., $\dot{q}_2(t;\omega)$ and $\dot{q}_3(t;\omega)$, due to their dependence on the random flow velocity V and the CFL width $w(\theta,t;\omega) = r_2 - r_1(\theta,t;\omega)$.

In lieu of example, in the numerical results reported below we assume the diffusion coefficients D_i in (4.1) to be the same and equal to D. Its value and the values of the remaining parameters used in our are model are reported in Table 4.1.

4.2.3 Statistical Representation of Random Surface

We represent spatio-temporal variations of the RBC-CFL interface,

$$r_1(\theta,t;\omega) = [\bar{r}_t + r_t'(t;\omega)][\bar{r}_\theta + r_\theta'(\theta;\omega)], \tag{4.11}$$

as the product of mutually uncorrelated temporal and angular fluctuations $r_t(t;\omega)$ and $r_\theta(\theta;\omega)$, respectively. A Reynolds decomposition is used to represent each of these fields, $r = \bar{r} + r'$, as the sum of its ensemble mean $\bar{r}$ and zero-mean fluctuations r'. Setting $\bar{r}_\theta = 1$ yields the mean and variance of the RBC-CFL interface: $\bar{r}_1 = \bar{r}_t$ and $\sigma_r^2 = \bar{r}_t^2\sigma_\theta^2 + \sigma_t^2(1 + \sigma_\theta^2)$. The coefficient of variation of the CFL width, $CV_w = \sigma_w/\bar{w}$, is given by

$$CV_w^2 = \left(\frac{\bar{r}_t}{\bar{w}}\right)^2 \sigma_\theta^2 + CV_t^2(1 + \sigma_\theta^2) \tag{4.12}$$

where $\overline{w} = r_2 - \overline{r}_1$ is the mean CFL width and σ_w is its standard deviation.

Since the random field $r'_\theta(\theta, \omega)$ is periodic, a truncated Fourier-type expansion

$$r'_\theta(\theta; \omega) \approx \sigma_\theta \sum_{n=-N_\theta}^{N_\theta} \nu_n(\omega) \mathrm{e}^{-in\theta} \tag{4.13}$$

provides its natural representation. Here the eigenvalues $\nu_n(\omega)$ are complex zero-mean random variables, whose real and imaginary parts are mutually independent for all n. Each has zero mean and variance $\sigma_n^2 = C_n/4$, where

$$C_n = \frac{1}{\pi} \int_0^{2\pi} C_\theta^p \cos(n\theta) \mathrm{d}\theta, \qquad -N \le n \le N \tag{4.14}$$

are coefficients of the Fourier cosine expansion of a 2π-periodic covariance function C_θ^p of the random field $r'_\theta(\theta, \omega)$. It is constructed as follows. First, we note that statistics of $r'_\theta(\theta; \omega)$ are rotationally invariant on the circle, such that a covariance function C_θ is

$$\langle r'_\theta(\theta_1; \omega) r'_\theta(\theta_2; \omega) \rangle = C_\theta(\Delta_\theta), \qquad \Delta_\theta = |\theta_1 - \theta_2|. \tag{4.15}$$

Then C_θ^p is constructed by extending the covariance function C_θ of the random field $r'_\theta(\theta, \omega)$ to a 2π-periodic periodic domain. We employ a Gaussian covariance function $C_\theta(\Delta_\theta) = \exp(-\Delta_\theta^2/l_\theta^2)$ with the correlation length l_θ. The decay of the Fourier cosine coefficients C_n determines the number of terms N_θ in the expansion (4.13) that is required to achieve a given truncation error. As the correlation length l_θ decreases, N_θ increases.

We represent the random field $r'_t(t; \omega)$ via a truncated Karhunen-Loéve expansion,

$$r_t(t, \omega) = \sigma_t \sum_{m=1}^{N_t} \sqrt{\lambda_m} f_m(t) Y_m(\omega), \qquad (4.16)$$

where $Y_m(\omega)$ $(m \geq 1)$ are independent random variables, and λ_m and $f_m(t)$ are respectively the eigenvalues and eigenfunctions of Fredholm equations,

$$\int_0^T \rho_t(t, t') f_m(t') \mathrm{d}t' = \lambda_m f_m(t), \qquad m \geq 1. \qquad (4.17)$$

For an exponential correlation function $\rho_t(t, t') = \exp(-|t - t'|/l_t)$ with the correlation length $l_t > 0$, the eigenvalue problems (4.17) admit an analytical solution [24],

$$\lambda_m = \frac{2l_t}{l_t^2 \omega_m^2 + 1}, \qquad f_m = \frac{l_t \omega_m \cos(\omega_m t) + \sin(\omega_m t)}{\sqrt{(l_t^2 \omega_m^2 + 1) T/2 + l_t}} \qquad (4.18)$$

where ω_m are solutions of $(l_t^2 \omega^2 - 1) \sin(\omega T) = 2 l_t \omega \cos(\omega T)$ and $m \geq 1$. The truncation error of the Karhunen-Loéve expansion (4.16) depends on the correlation length l_t. The smaller the correlation length, the more terms N_t are necessary to represent the random field $r'(t, \omega)$ with a given degree of accuracy.

Within the statistical framework adopted here, the random RBC-CFL interface is characterized by four parameters: variances σ_θ^2 and σ_t^2, and correlation lengths l_θ and l_t. Experimental data, such as those reported in [67], can be used to estimate these statistics. Table 4.1 contains the values of these parameters used in our simulations.

Table 4.1: Parameters and their values used in the model.

Parmeters	Symbol	Value	Units	Source
Vessel radius	r_2	23.3	μm	[2]
Blood lumen width	$r_1 = \bar{r}_1 + r'$	random	μm	-
Mean cell free layer width	$\bar{w} = r_2 - \bar{r}_1$	2.73 or 3.22	μm	[2]
Endothelial cell width	$r_3 - r_2$	2.5	μm	[70]
Tissue layer width	$r(\infty) - r_3$	250.0	μm	-
Diffusion coefficient	D	3300.0	μm^2 / s	[54]
Control NO production rate	$\dot{q}^{\star}_{NO}$	$2.65 \cdot 10^{-14}$	μmol / (μm^{2}s)	[54]
NO scavenging rate at Hc 40%	k_{sys}	382.5	1 / s	[32]
NO scavenging rate in endothelium	k_{EC}	0.1	1 / s	[55]
NO scavenging rate in tissue	k_T	0.1	1 / s	[55]
Plasma viscosity	μ_p	1.2	cP	[71]
Reference wall shear stress	$\tau_{w,ref}$	2.4	Pa	[56]

4.3 Numerical Solution

4.3.1 Mapping onto Deterministic Domain

We introduce a new coordinate system (ξ_1, ξ_2), in which the original stochastic domain $\mathcal{D}$ maps onto a rectangle $B = \{(\xi_1, \xi_2) : -1 \leq \xi_1 \leq 1, 0 \leq \xi_2 \leq 2\pi\}$. A mapping $\mathcal{D} = \cup_{i=1}^{4} E^i \to V$ is accomplished analytically by the coordinate transformation

$$r = r_{i-1} + \frac{\xi_1 + 1}{2}(r_i - r_{i-1}), \quad \theta = \xi_2; \quad (r, \theta) \in E^i \tag{4.19}$$

where $i = 1, \ldots, 4$ and $r_0 = 0$. The random RBC-CFL interface $r_1(\theta, t; \omega)$ is represented by the expansions described above.

4.3.2 Transformed Stochastic Equations

The mapping (4.19) renders the transformation Jacobian

$$J(\xi_1, \xi_2, \omega) \equiv \frac{\partial(\xi_1, \xi_2)}{\partial(r, \theta)} = J[\xi_1, \xi_2, Y_1(\omega), \cdots, Y_K(\omega)] \tag{4.20}$$

and other related metrics stochastic, i.e., dependent on a set of $K = 2N_\theta + N_t$ independent random variables $\{Y_i(\omega)\}_{i=1}^{K}$. The first N_t variables $Y_1, \ldots, Y_{N_t}$ coincide with those introduced in (4.16) and the remaining $2N_\theta$ variables represent their counterparts in (4.13), such that $Y_{N_t+1} = \nu_{-N_\theta}, \ldots, Y_K = \nu_{N_\theta}$. Consequently, the deterministic reaction-diffusion equations (4.1) are transformed into stochastic

equations of the form (Appendix B)

$$\frac{\partial C_{\mathrm{NO}}}{\partial t} = \sum_{i,j=1}^{2} \frac{\partial}{\partial \xi_i} \left(D A_{ij} \frac{\partial C_{\mathrm{NO}}}{\partial \xi_j} \right) - k C_{\mathrm{NO}} \qquad (4.21)$$

where the random coefficients A_{11}, $A_{12} = A_{21}$, and A_{22} are given by (B.2) in the Appendix B.

These stochastic differential equations on the deterministic domain B can be solved with a variety of well-established techniques, including perturbation-based moment equations [46, and the references therein], stochastic finite elements [72], and stochastic collocation on sparse grids [24, and the references therein]. In the subsequent numerical simulations we employ the latter approach (Appendix A.2).

4.4   Simulation Results and Discussion

Solutions of the stochastic system of transport equations (4.1)–(4.3) are given in terms of statistical moments of the dependent variables. Ensemble means, e.g., mean NO concentration $\bar{C}_{\mathrm{NO}}$, serve as unbiased predictors of the system behavior; variances, e.g., NO concentration variance σ_C^2, act as a measure of predictive uncertainty.

4.4.1   Data-driven model parameterization

The CFL width measurements [2] are used to construct a probabilistic model for the random input parameter $w(\theta, t; \omega) = r_2 - r_1$ in which the random RBC-CFL interface $r_1(\theta, t; \omega)$ is given by (4.11). These data, which represent

temporal fluctuations of w at a single spatial location (say, $\theta = 0$), give rise to the histogram and auto-correlation reported in Figs. 4.2 and 4.3, respectively. This histogram (and the obvious fact that the CFL width is both non-negative and smaller than the vessel radius r_2) indicates that the random field $w(\theta, t; \omega)$ is non-Gaussian. We fit the histogram in Fig. 4.2 with a beta distribution $f_w(W) = \mathrm{B}^{-1} r_2^{1-\alpha-\beta} W^{\alpha-1} (r_2 - W)^{\beta-1}$, where $\mathrm{B}(\alpha, \beta) = \Gamma(\alpha + \beta)/[\Gamma(\alpha)\Gamma(\beta)]$ is the beta function, $\Gamma(\cdot)$ is the complete gamma function, $0 \le W \le r_2$, and $\alpha > 0$ and $\beta > 0$ are shape parameters. Setting $\alpha = 4.358$ and $\beta = 32.9$ provides the best data fit, resulting in the mean CFL width $\bar{w} = 2.73$ μm. The auto-correlation data in Fig. 4.3 were fitted with an exponential correlation function $\rho(t, t') = \exp(-|t - t'|/l_t)$, yielding the correlation length $l_t = 0.007$ s.

Another data set reported in [2] contains information about temporal fluctuations of the CFL width $w(0, t; \omega)$ after Dextran infusion. Fitting the beta distribution ($\alpha = 3.464$ and $\beta = 21.5$) and the exponential correlation function to these data leads to estimates of the mean CFL width $\bar{w} = 3.22$ μm and the correlation length $l_t = 0.008$ s.

Experimental limitations preclude data acquisition at multiple azimuths θ, which requires us to postulate a probabilistic model for $r_\theta(\theta; \omega)$. In analogy with its temporal counterpart $r_t(t; \omega)$, we chose $r_\theta(\theta; \omega)$ to have the beta distribution with unit mean and variance σ_θ^2 and the exponential correlation function with correlation length l_θ. In this formulation (4.12), the amplitude of spatio-temporal (in the angular coordinate θ and time t) fluctuations of both the RBC-CFL interface
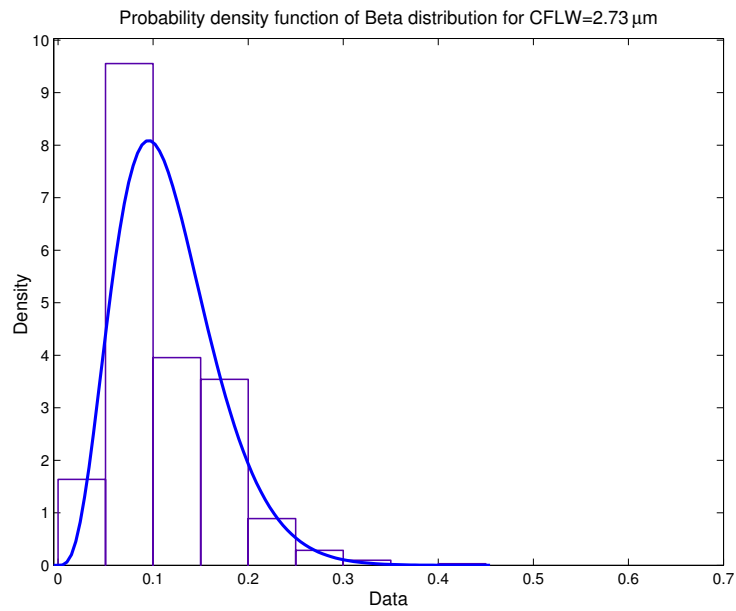
(a)
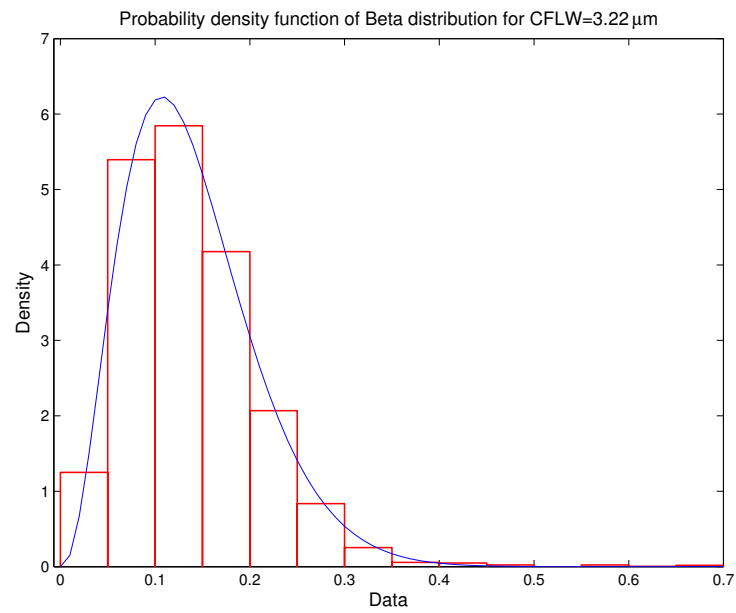
(b)

Figure 4.2: Frequency distribution of the data reported in [2] and the fitted β-distribution for (a) 2.73 μm and (b) 3.22 μm.
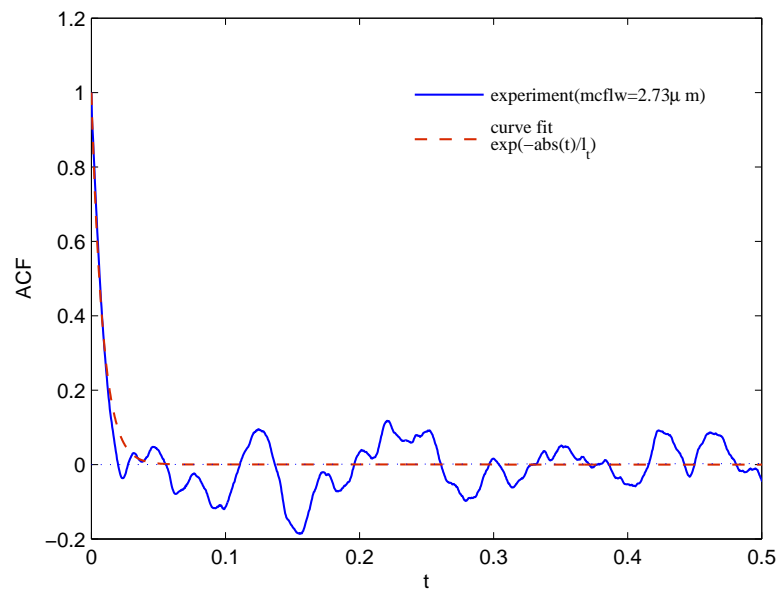
Figure 4.3: Auto-correlation of the data reported in [2] (solid line) and the fitted exponential correlation function (dashed line).

$r_1(\theta, t; \omega)$ and CFL width $w(\theta, t; \omega) = r_2 - r_1$ increases with the variances σ_θ^2 and σ_t^2, while the smoothness of these fluctuations increases with the correlation lengths l_θ and l_t. This behavior, which reflects chaotic motion of RBCs in the blood core, is demonstrated by two representative realizations of the random CFL width shown in Fig. 4.4.
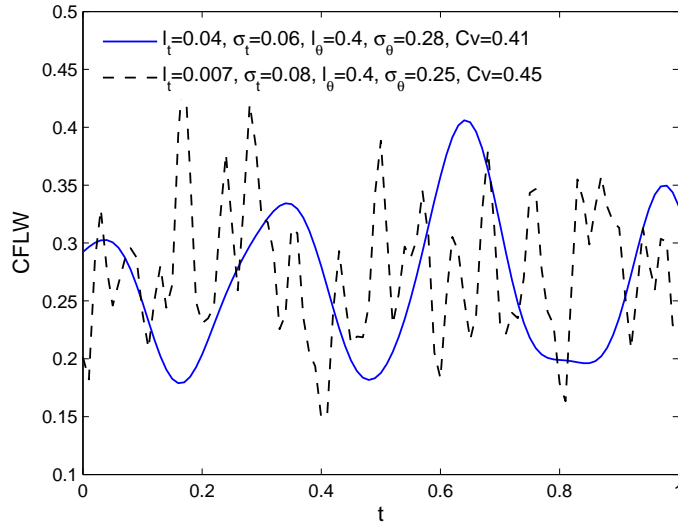
Figure 4.4: Realizations of temporal fluctuations of the CFL width w at angular coordinate $\theta = 0.0$.

4.4.2 Random fluctuations of wall shear stress

The CFL width w in (4.10) is inversely proportional to the wall shear stress (WSS) τ_w. Hence the random spatio-temporal fluctuations in w induce corresponding fluctuations in τ_w, as shown in Fig. 4.5. Here and below we used the values of the edge velocity $V_e = 0.54mm/s$ and the corresponding pressure gradi-
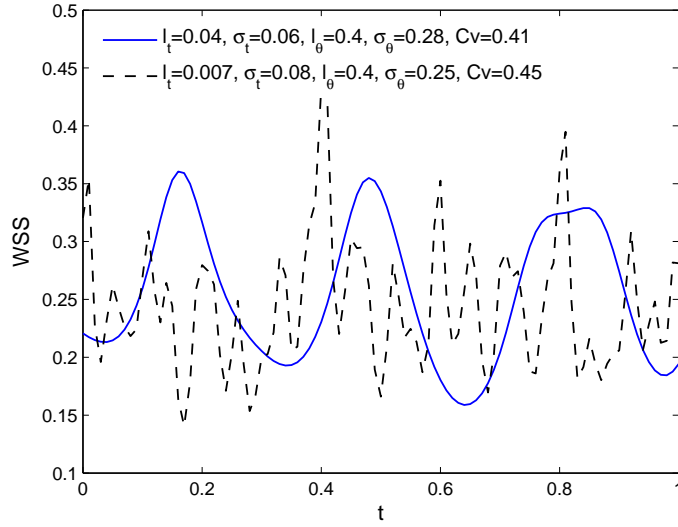
Figure 4.5: Realizations of temporal fluctuations of wall shear stress τ_w at angular coordinate $\theta = 0.0$.

ent $J = 2.15 \times 10^4$ computed by fitting the smooth-wall model to the experimentally observed peak NO concentration of 11.2 nM.

The statistics commonly available from experimental studies similar to [66, 67, 2] is the coefficient of variation of the CFL width, $\text{CV}_w = \sigma_w/\bar{w}$. Figure 4.6 shows how the mean WSS $\bar{\tau}_w$, normalized with the smooth-vessel WSS $\tau_w^\star$, increases with CV_w. (Recall that the fixed/smooth boundaries of the CFL correspond to $\text{CV}_w = 0$ and $\bar{\tau}_w/\tau_w^\star = 1$.) The rate of growth of the mean WSS depends on the model's statistical parameters, some of which, especially l_θ, are not found in the experiments [66, 67, 2]. Fortunately, Fig. 4.6 reveals that the mean WSS is nearly insensitive to l_θ, being dominated by the temporal fluctuations statistics that are more readily measurable.
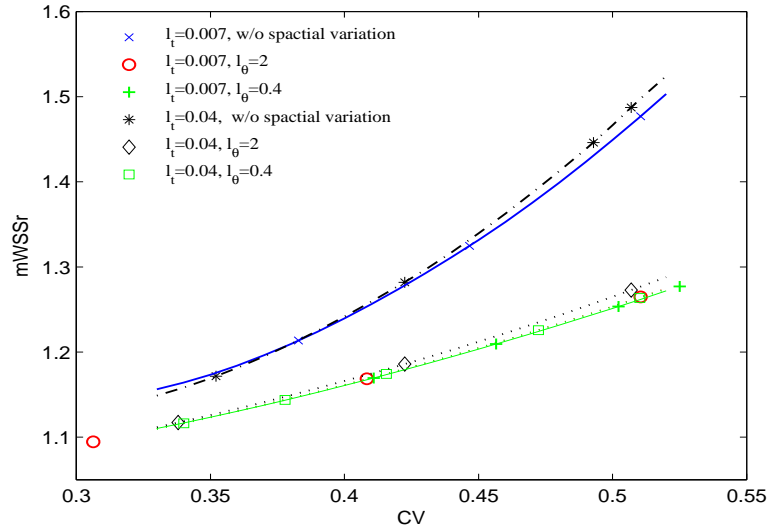
Figure 4.6: Mean WSS, normalized with the smooth-vessel WSS $\tau_w^\star$, (and mean NO production rate, normalized with the control production rate $\dot{q}^\star$) as a function of the coefficient of variation ($CV_w = \sigma_w/\bar{w}$) of the CFL width for several combinations of constitutive statistical parameters.

4.4.3 NO production rate

It follows from (4.10) that the NO production rate by the endothelium, $\dot{q}_2$, is directly proportional to the WSS. When normalized by the control production rate $\dot{q}^\star$, it is equal to the ratio $\tau_w/\tau_w^\star$. In other words, the statistics of the ratios $\dot{q}_2/\dot{q}^\star$ and $\tau_w/\tau_w^\star$ coincide. Therefore, Fig. 4.6 also demonstrates how the mean NO production rate by the endothelium, $\bar{\dot{q}}_2/\dot{q}^\star$, increases with the coefficient of variation of the CFL width, CV_w.

4.4.4 Mean profiles of NO concentration

Unless specified otherwise, the results reported below correspond to the hematocrit-dependent reaction rate k_1 in (4.4) given by the constitutive model (4.8)–(4.9). We start by computing a (deterministic) reference NO concentration $c_{\mathrm{NO}}^\star(r)$ as a solution of (4.1)–(4.3) with smooth (constant) interfaces r_1 and r_2. It serves as an initial condition for transient stochastic simulations.

The mean concentration profiles computed with these simulations, $\bar{C}_{\mathrm{NO}}(r)$, are exhibited in Figure 4.7. While the NO production rates ($\dot{q}_2$ and $\dot{q}_3$) on both sides of the endothelium ($r = r_2$ and r_3) are the same, the NO scavenging rate in the RBC core ($0 \leq r \leq r_1$) is higher than that in the muscle tissue ($r > r_3$). That is why the peak NO concentration is at the endothelium surface facing the tissue ($r = r_3$).

Figure 4.7 also reveals that random fluctuations of the CFL width increase
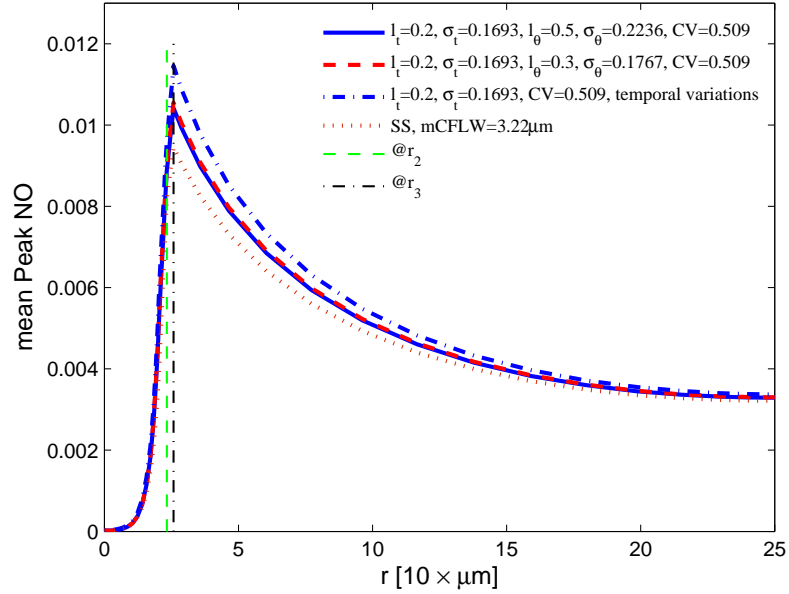
Figure 4.7: Mean NO Concentraion for temporal and spacial variation of CFL.

the NO availability relative to that predicted by the model that ignores them. This is to be expected, since these fluctuations enhance the NO production by the endothelium (Fig. 4.6). NO production and availability increase with the the degree of roughness of the random RBC-CFL interface $r_1(\theta, t; \omega)$: the higher CV_w and/or the smaller the correlation lengths l_t and l_θ, the rougher the interface is.

The simulation results reported in Table 4.2 demonstrate the relative importance of temporal and angular fluctuations of the CFL width on NO availability. The latter is reported in terms of the ratio of the peak NO concentrations, $\mathcal{R} = (\bar{C}_{\max} - C^\star_{\max})/C^\star_{\max}$, where $C^\star_{\max} = C^\star_{NO}(r_3)$ and $\bar{C}_{\max} = \bar{C}_{NO}(r_3)$. Larger values of $\mathcal{R}$ indicate the stronger impact of the CFL width fluctuations.

Table 4.2: Summary of simulation results.

Case	D_t	D_θ	σ_t	σ_θ	l_t	l_θ	Cv	$\mathcal{R}$	$\bar{w}$ (μm)
temporal variation	6		0.06		0.2		0.464	14.2	2.73
	6				0.2		0.443	12.4 **	2.73
	10				0.1		0.443	13.2 **	2.73
	6		0.08		0.2		0.525	20.4	3.22
	6				0.2		0.509	18.3 **	3.22
temporal and	6	4	0.06	0.34	0.2	1	0.448	10.7	2.73
spacial variation	6	6	0.06	0.27	0.2	0.6	0.44	9.1	2.73
	6	4	0.08	0.35	0.2	1	0.519	12.4	3.22
	6	6	0.08	0.28	0.2	0.6	0.509	10.7	3.22
	10	5	0.06	0.3	0.2	0.7	0.509	11.8	2.73
	10	5	0.06	0.3	0.2	0.7	0.509	11.2	2.73*

*: degrading reaction rate is based on two layer velocity

**: value with curve fitting

4.4.5 Effect of constitutive models

The above-made estimates of NO production and availability rely on the NO scavenging rate $k_1(t; \omega)$ given by the constitutive law (4.8)–(4.9), which treats blood as a single-phase fluid. The alternative constitutive model for $k_1(t; \omega)$, which explicitly accounts for the CFL presence, is given by (4.6)–(4.7). Our simulations demonstrate that the difference between the mean peak NO concentrations predicted with the two models is less than 1 per cent (Table 4.2). This provides a confirmation of the robustness of our predictions of expected NO production and availability with respect to model selection for the scavenging rate.

4.4.6 Effect of dextran infusion

In the experiments reported in [2], infusion of a plasma expander dextran increases the average CFL width from $\bar{w} = 2.73$ μm to 3.22 μm. It also enhances fluctuations of the CFL width, increasing CV_w from 0.443 to 0.509 while leaving the correlation length l_t practically unchanged (it increases from 0.007 s before the dextran infusion to 0.008 s after). To match the decrease in the reported peak NO concentration from 11.2 nM to 9.5 nM, we recalculated the value of the pressure gradient $J = 2.15 \times 10^4$ and 1.72×10^4 Pa.

Figure 4.8 demonstrates that changing the mean CFL width (from 2.73 μm to 3.22 μm) does not significantly change the mean WSS, but has a more pronounced effect on the mean peak NO concentrations. The peak NO concentration

ratio $\mathcal{R}$ reported in Table 4.2 further emphasizes this effect.

4.4.7 Quantification of predictive uncertainty

Figure 4.9 shows that std NO concentration is increased with a higher control parameter σ_θ and a peak values is at the location r_3 (the endothelium surface toward tissue), which is the same point the mean NO peak value arise at.

4.5 Conclusions

We developed a computational framework to quantify the impact of uncertainty in the CFL width on the distribution of NO concentration. This is accomplished by treating the RBC-CFL interface (and the corresponding CFL width) as a space-time correlated random field. This surface is represented via Karhunen-Loéve and Fourier expansions. The differential equations describing blood flow and NO production and transport, defined on random simulation domains, were solved by using a stochastic collocation method.

Our analysis leads to the following major conclusions.

- Both NO production rate by the endothelium and NO scavenging by RBCs depend upon the CFL width. Random fluctuations in the CFL width results in random fluctuations of NO production and availability.

- Even though the NO concentration in microvascular systems depends on fluctuations of the WSS-induced NO production rate and the scavenging
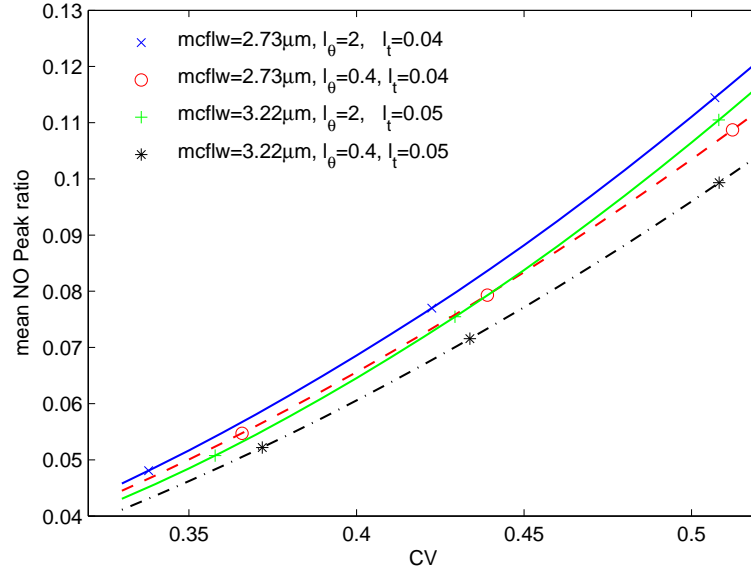
(a)
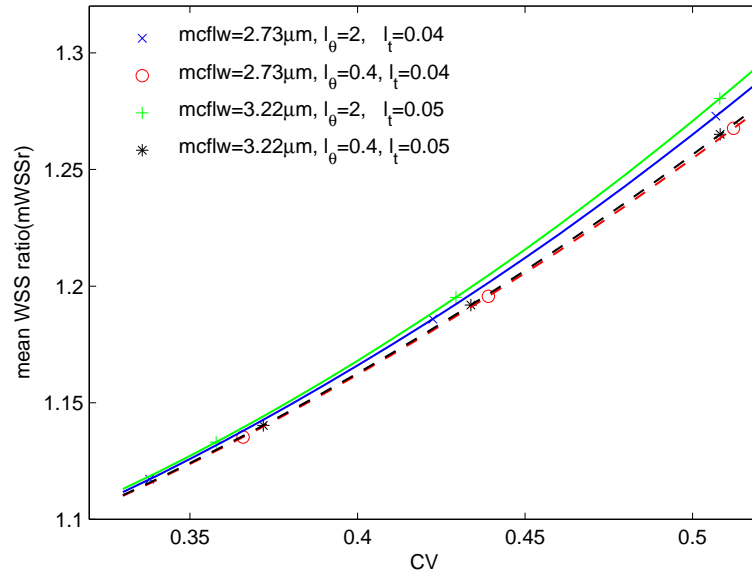
(b)

Figure 4.8: Mean NO peak ratio and mean Wall shear stress ratio for temporal and spatial variations of the CFL for the mean CFL width 2.73μm and 3.22μm.
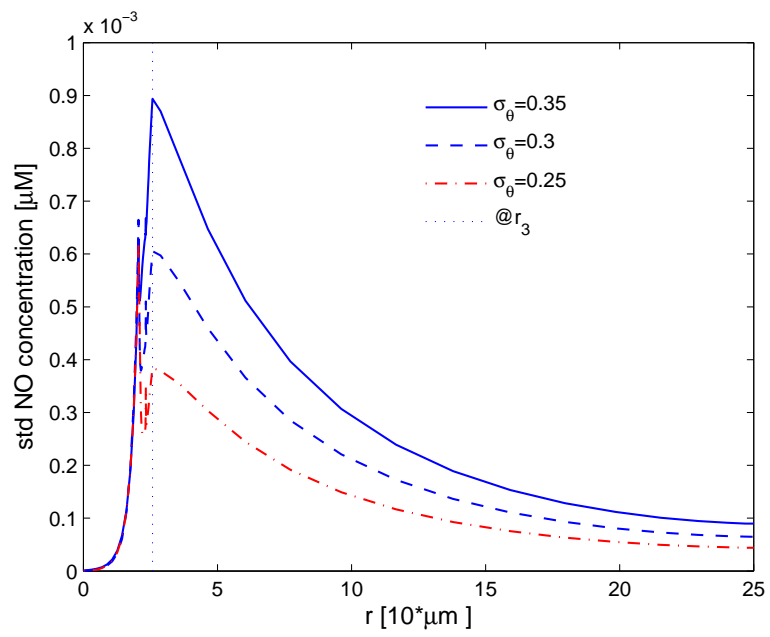
Figure 4.9: std NO Concentration with different correlation lengthsl_θ.

rate related to velocity profile and hematocrit, the effect of fluctuations of the CFL width on the latter is smaller than that on the former. Also, the effect of the mean value of the CFL width on NO concentration is significant.

- Random temporal fluctuations of the CFL width increase the NO peak concentration relative to its values predicted with a model that ignores such fluctuations.

- Dextran infusion increases not only the mean CFL width but also its correlation length.

Chapter 5

Conclusions

This dissertation leads to the following major conclusions:

1. The mean pressure gradient is constant and unaffected by the endothelium roughness. Uncertainty in (randomness of) the endothelium surface manifests itself in pressure fluctuations about the mean, as quantified by the standard deviation σ_p.

2. The overall effect of endothelium roughness is to reduce the mean blood flow velocity relative to its counterpart corresponding to the assumption of smooth endothelium ($\sigma_s = 0$). For a given σ_s, the mean velocity decreases as l_s becomes smaller, i.e., the endothelium surface becomes more irregular.

3. The decrease in mean velocity with increasing endothelium roughness translates into the corresponding decrease in the volumetric flow rate. The volumetric flow rate decreases as the roughness amplitude (standard deviation)

σ_s increases and/or the correlation length l_s decreases.

4. The mean shear stress increases with both the magnitude of the endothelium fluctuations (its standard deviation σ_s) and its correlation length l_s. Boundary effects (deviation from the fully-developed flow regime, wherein the shear stress statistics are constant) extend further inside the flow chamber as σ_s increases and/or l_s decreases.

5. The blood viscosity, inferred from in vivo experiments via the Poiseuille law, depends not only on blood properties but also on the statistical parameters characterizing the endothelium roughness (σ_s and l_s). The effective blood viscosity increases as σ_s increases and/or l_s decreases.

6. Random roughness reduces the volumetric flow rate and gets larger the magnitude in fluctuations of the velocity components; this reduction becomes more pronounces as the roughness' variance increases and/or its correlation length decreases.

7. The the peak of predictive uncertainty is shifted from the channels centerline towards its random wall. The location of maximum predictive uncertainty is insensitive to the roughness' variance but is affected by its correlation length. The location in maximum magnitude of fluctuations moves toward the random surface with smaller correlation length(rougher).

8. Both NO production rate by the endothelium and NO scavenging by RBCs

depend upon the CFL width. Random fluctuations in the CFL width results in random fluctuations of NO production and availability.

9. Even though the NO concentration in microvascular systems depends on fluctuations of the WSS-induced NO production rate and the scavenging rate related to velocity profile and hematocrit, the effect of fluctuations of the CFL width on the latter is smaller than that on the former. Also, the effect of the mean value of the CFL width on NO concentration is significant.

10. Random temporal fluctuations of the CFL width increase the NO peak concentration relative to its values predicted with a model that ignores such fluctuations.

11. Dextran infusion increases not only the mean CFL width but also its correlation length.

Appendix A

Stochastic Methods

Let $\{\Psi_m(\mathbf{Y})\}_{m=0}^M$ denote a set of multidimensional orthogonal polynomials of the random vector $\mathbf{Y}(\omega) \equiv (Y_1, \dots, Y_K)^T$. The polynomials are chosen to have the ensemble means $\overline{\Psi}_0 = 1$ and $\overline{\Psi}_k = 0$ $(k \geq 1)$ and to satisfy the orthogonality condition

$$\langle \Psi_i \Psi_j \rangle = \langle \Psi_i^2 \rangle \delta_{ij} \tag{A.1}$$

where the $\langle \cdot \rangle$ operator is defined by

$$\langle \Psi_i \Psi_j \rangle \equiv \int \Psi_i(\mathbf{Y}) \Psi_j(\mathbf{Y}) W(\mathbf{Y}) \mathrm{d}Y_1 \dots \mathrm{d}Y_K, \tag{A.2}$$

δ_{ij} is the Kronecker delta and $W(\mathbf{Y})$ is a weight function corresponding to a given polynomial type. The size of the polynomial set, M, is determined by the "stochastic dimension" K and the order P of polynomials Ψ_k, according to

$$M = \frac{(K+P)!}{K!P!} - 1. \tag{A.3}$$

Polynomial chaos expansions (PCEs) represent a system state, e.g., $u(\boldsymbol{\xi}, \omega)$, a random field whose ensemble statistics are to be determined, as a series

$$u(\boldsymbol{\xi}, \omega) = \sum_{k=0}^{M} \hat{u}_k(\boldsymbol{\xi}) \Psi_k[\mathbf{Y}(\omega)]. \tag{A.4}$$

With the representation of system response $u(\xi, \omega)$ as Polynomial chaos expansions, we adopt Stochastic Galerkin Method and Stochastic Collocation Method to solve the problems with Uncertainty.

A.1 Stochastic Galerkin Method

A good introduction to stochastic finite elements can be found in [3]. Here we provide a brief description. Let $\mathcal{L}(\boldsymbol{\xi}, \omega; u)$ denote a stochastic differential operator acting on $u(\boldsymbol{\xi}, \omega)$. Consider a stochastic partial differential equation (PDE)

$$\mathcal{L}(\boldsymbol{\xi}, \omega; u) = f(\boldsymbol{\xi}, \omega), \tag{A.5}$$

where f is a (random) source function. Substituting the polynomial chaos expansion of u, Eq. A.4, into Eq. A.5 yields

$$\mathcal{L}\left(\boldsymbol{\xi}, \omega; \sum_{k=0}^{M} u_k \Psi_k\right) = f(\boldsymbol{\xi}, \omega). \tag{A.6}$$

Multiplying both sides of Eq. A.6 with Ψ_i and taking the mean, while accounting for the orthogonality condition in Eq. A.1, yields a Galerkin projection onto the i-th basis polynomial Ψ_i,

$$\left\langle \mathcal{L}\left(\xi, \omega; \sum_{k=0}^{M} u_k \Psi_k\right), \Psi_i \right\rangle = \langle f(\xi, \omega), \Psi_i \rangle, \qquad i = 0, \ldots, M. \tag{A.7}$$

Here the inner product $\langle a, b \rangle$ between two functions $a(\mathbf{Y})$ and $b(\mathbf{Y})$ is defined in terms of the ensemble average $\overline{ab}$ in Eq. A.1. Equation A.7 gives rise to a system of $M + 1$ deterministic PDEs for $u_k(\mathbf{x})$ $(k = 0, \ldots, M)$.

A.2   Stochastic Collocation Method

Stochastic Collocation Method requires the solution of a set of decoupled equations as Monte Carlo Method.

Consider a stochastic partial differential equation (PDE)

$$\mathcal{L}(\boldsymbol{x}, \xi(\omega); u) = f(\boldsymbol{x}, \xi(\omega)), \tag{A.8}$$

The solution to SPDE is approximated by using Lagrange formula,

$$u(\boldsymbol{x}, \boldsymbol{\xi}(\omega)) = \sum_{k=0}^{Nq} u_k(\boldsymbol{x}, \boldsymbol{\xi}(\omega)^k) L_k(\boldsymbol{\xi}(\omega)), \tag{A.9}$$

where, $u_k(\boldsymbol{x}, \boldsymbol{\xi}(\omega)^k)$ is the solution at the set of collocation points $\{\boldsymbol{\xi}^k\}_{k=0}^{Nq}$, L_i is the Lagrane polynomial of (Nq+1) order and $L_i(\xi_j) = \delta_{ij}$. This Lagrange formula(Equation A.9) is putting into the inner product formula(Eq. with the basis functions chosen to be dirac delta functions $\delta(\xi - \xi^k)$, and then (Nq+1) uncoupled deterministic problems is obtained at the collocation points.

$$\mathcal{L}(\boldsymbol{x}, \xi^k(\omega); u_k) = f(\boldsymbol{x}, \xi^k(\omega)), \qquad \text{for k=0, ... , Nq} \tag{A.10}$$

Once the solutions at a set of collocation points is obtained, Statistics of the

solutions can be computed by using the corresponding quadrature rule.

$$\overline{u}(\boldsymbol{x}) = \int_{\Gamma} u(\boldsymbol{x}, \boldsymbol{\xi})p(\boldsymbol{\xi})d\boldsymbol{\xi} \approx \sum_{k=1}^{Nq} u(\boldsymbol{x}, \boldsymbol{\xi}^k)w_k \qquad (\text{A.11})$$

$$\sigma_u^2(\boldsymbol{x}) = \int_{\Gamma} [u(\boldsymbol{x}, \boldsymbol{\xi}) - \overline{u}(\boldsymbol{x})]^2 p(\boldsymbol{\xi})d\boldsymbol{\xi} \approx \sum_{k=1}^{Nq} u(\boldsymbol{x}, \boldsymbol{\xi}^k)^2 w_k - \overline{u}(\boldsymbol{x})^2 \qquad (\text{A.12})$$

where, $\{w_k\}_{k=1}^{Nq}$ is a set of weights corresponding to the set of quadrature points $\{\boldsymbol{\xi}^k\}_{k=0}^{Nq}$

Appendix B

Transformed Transport Equations

A general transformation of coordinates $\xi_i(x_1, x_2)$ transforms the Fickian flux $\mathbf{F}(\mathbf{x}) = -D\nabla_{\mathbf{x}} C_{\mathrm{NO}}$ into a vector $\mathbf{F}(\boldsymbol{\xi})$ whose contravariant components F^1 and F^2 are given by

$$F^i = D\frac{1}{J}\sum_{k=1}^{2} A_{ik}\frac{\partial C_{\mathrm{NO}}}{\partial \xi_k}, \qquad i = 1, 2 \tag{B.1}$$

where J is the transformation Jacobian (4.20) and

$$A_{11} = \left(\frac{\partial x_2}{\partial \xi_2}\right)^2 + \left(\frac{\partial x_1}{\partial \xi_2}\right)^2, \tag{B.2a}$$

$$A_{12} = A_{21} = -\frac{\partial x_2}{\partial \xi_1}\frac{\partial x_2}{\partial \xi_2} - \frac{\partial x_1}{\partial \xi_1}\frac{\partial x_1}{\partial \xi_2}, \tag{B.2b}$$

$$A_{22} = \left(\frac{\partial x_2}{\partial \xi_1}\right)^2 + \left(\frac{\partial x_1}{\partial \xi_1}\right)^2. \tag{B.2c}$$

Furthermore,

$$\nabla_{\mathbf{x}} \cdot \mathbf{F} = \frac{1}{J}\left(\frac{\partial F^1}{\partial \xi_1} + \frac{\partial F^2}{\partial \xi_2}\right) \equiv \frac{1}{J}\nabla_{\boldsymbol{\xi}} \cdot \mathbf{F}. \tag{B.3}$$

Substituting (B.1)–(B.3) into (4.1) leads to (4.21).

Appendix C

Spectral Element Method

C.1 Galerkin Formulation for Spectral Element Method

The spectral methods in single element domain can be extended to a multi-element domain to compute problems in more complex domain, problems with coordinate singularities, and problems with discontinuous coefficients or solutions. First, we can use the weak form of the governing equations in each element domain, that is Galerkin based methods [26, 27, 28, 29]. The Galerkin approximation have natural coupling that follows from the weak form. This is Spectral Element Method(SEM) similar to Finite Element Method.

We describe how to formulate the Galerkin approximation of Poisson equation

C.1.1   Formulation

Consider one dimensional Poisson's equation in a domain $E = \{x : 0 \leq x \leq 1\}$ and $E = \sum_{e=1}^{N} E^e$.

The strong form of poisson's equation is stated as follows:

$$\mathbb{L}(\psi) \equiv \nabla^2 \psi + s = 0, \qquad \psi(0) = g_D, \qquad \frac{\partial \psi}{\partial x} = g_N \tag{C.1}$$

The weak form is derived by multiplying equation (C.1) by a test functon ϕ.

$$(\phi, \mathbb{L}(\psi)) = \int_0^1 \phi \left(\frac{\partial^2 \psi}{\partial x^2} + s \right) dx = 0, \tag{C.2}$$

Then integration by parts states that

$$\int_0^1 \frac{\partial \phi}{\partial x} \frac{\partial \psi}{\partial x} dx = \int_0^1 \phi s \, dx + \left[\phi \frac{\partial \psi}{\partial x} \right]_0^1$$

$$= \int_0^1 \phi s \, dx + \phi(1) g_N \tag{C.3}$$

In spectal/finite element method a whole domain E consists in N finite elements. Equation (C.3) is represented as

$$\int_0^1 \frac{\partial \phi}{\partial x} \frac{\partial \psi}{\partial x} dx = \sum_{e=1}^{N} \int_{E^e} \frac{\partial \phi}{\partial x} \frac{\partial \psi}{\partial x} dx$$

$$= -\sum_{e=1}^{N} \int_{E^e} \phi \frac{\partial^2 \psi}{\partial x^2} dx + \sum_{e=1}^{N} \left[\phi \frac{\partial \psi}{\partial x} \right]_{E_L^e}^{E_R^e}$$

$$= -\int_0^1 \phi \left(\frac{\partial^2 \psi}{\partial x^2} \right) dx + \sum_{e=1}^{N} \left[\phi \frac{\partial \psi}{\partial x} \right]_{E_L^e}^{E_R^e} \tag{C.4}$$

where, L and R are the left and right end in a element E^e. ϕ_R^e and ϕ_L^{e+1} at the interface between two elements (E^e and E^{e+1}) are the same.

By substituting equation (C.4) into equation (C.3), the following equation is derived

$$
-\int_0^1 \phi \left(\frac{\partial^2 \psi}{\partial x^2} + s \right) dx - \left[\phi \frac{\partial \psi}{\partial x} \right]_{E_L^1} + \sum_{e=1}^{N-1} \left[\phi \frac{\partial \psi}{\partial x} \bigg|_{E_R^e} - \phi \frac{\partial \psi}{\partial x} \bigg|_{E_L^{e+1}} \right]
$$
$$
\left[\phi \frac{\partial \psi}{\partial x} \bigg|_{E_R^N} - \phi(1)g_N \right] = 0 \tag{C.5}
$$

The second term and the last term are zero since E_L^1 is a Dirichlet boundary and E_R^N is a Neumann boundary. The third term stands for the jump in the derivative at the interface between two elements. This jump/flux condition is used in chapter 4. When the derivative of function is continuous such that

$$
\phi \frac{\partial \psi}{\partial x} \bigg|_{E_R^e} = \phi \frac{\partial \psi}{\partial x} \bigg|_{E_L^{e+1}} , \tag{C.6}
$$

the only first terms is not zero and equation (C.5) becomes the standard weighted residual. No jump condition is used in chapter 3 and 4.

It is convenient to impose a jump condition at the interface between elements in finite/spectral element method [26, 27, 28, 29].

C.1.2 2D SEM for Transformed equations

Consider two-dimensional Potential equation with Dirichlet boundary condition in a domain $\Omega = \sum_{k=1}^{K} \Omega^k$.

$$\mathbb{L}(\varphi) \equiv \nabla^2 \varphi - s = 0, \qquad (x, y) \in \Omega \tag{C.7}$$

$$\varphi = \varphi_b, \qquad \mathbf{x} \in \partial\Omega \tag{C.8}$$

Weak Form is stated as

$$(\phi, \mathbb{L}(u)) = \iint_{\Omega} \phi \left(\nabla^2 \varphi - s \right) dxdy = 0, \tag{C.9}$$

where ϕ is a smooth function. Applying Green's identity, equation (C.9) is derived as

$$\iint_{\Omega} \phi \nabla^2 \varphi \, dxdy = \int_{\partial\Omega} \phi \frac{\partial \varphi}{\partial n} dL - \iint_{\Omega} \nabla\varphi \cdot \nabla\phi \, dxdy, \tag{C.10}$$

Equation (C.10) is represented as the form of the sum of elements(Ω^k).

$$\sum_{k=1}^{K} \left(\int_{\partial\Omega^k} \phi \frac{\partial\varphi}{\partial n} dL - \iint_{\Omega^k} \nabla\varphi \cdot \nabla\phi \, dxdy \right) = \sum_{k=1}^{K} \left(\iint_{\Omega^k} s\phi \, dxdy \right) \tag{C.11}$$

For convenience, the left and right side represent as

$$I_1^k = \left(\int_{\partial\Omega^k} \phi \frac{\partial\varphi}{\partial n} dL - \iint_{\Omega^k} \nabla\varphi \cdot \nabla\phi \, dxdy \right)$$
$$I_2^k = \left(\iint_{\Omega^k} s\phi \, dxdy \right) \tag{C.12}$$

We first map the element Ω^k onto the reference square($E = \{(\xi, \eta) | \quad -1 \leq \xi \leq 1, \quad -1 \leq \eta \leq 1\}$) by a mapping $\mathbf{x} = \mathbf{X}(\xi, \eta)$

Through a mapping, Equations (C.12) is derived as

$$I_2^k = \left(\int_{-1}^1 \int_{-1}^1 J^k s\phi \, d\xi d\eta \right) \tag{C.13}$$

$$
\begin{aligned}
I_1^k &= \left(\int_{\partial\Omega^k} \phi \frac{\partial\varphi}{\partial n} dL - \iint_{\Omega^k} \nabla\varphi \cdot \nabla\phi \, dxdy \right) \\
&= \int_{\xi=-1}^1 \phi F^2 \Big]_{\eta=-1}^1 d\xi + \int_{\eta=-1}^1 \phi F^1 \Big]_{\xi=-1}^1 d\eta \\
&\quad - \int_{-1}^1 \int_{-1}^1 \left(F^1 \phi_\xi + F^2 \phi_\eta \right) d\xi d\eta
\end{aligned} \tag{C.14}
$$

where the gradient in the mapped coordinate is

$$\nabla\varphi = \frac{1}{J}\left[\left(\frac{\partial y}{\partial \eta}\mathbf{i} - \frac{\partial x}{\partial \eta}\mathbf{j} \right) \frac{\partial\varphi}{\partial\xi} - \left(\frac{\partial y}{\partial\xi}\mathbf{i} - \frac{\partial x}{\partial\xi}\mathbf{j} \right) \frac{\partial\varphi}{\partial\eta} \right]. \tag{C.15}$$

$$
\begin{aligned}
\nabla\varphi \cdot \nabla\phi &= \frac{1}{J}\left[\left(A\varphi_\xi - B\varphi_\eta \right)\phi_\xi + \left(C\varphi_\eta - B\varphi_\xi \right)\phi_\eta \right] \\
&= \frac{1}{J}\left(F^1\phi_\xi + F^2\phi_\eta \right)
\end{aligned} \tag{C.16}
$$

with

$$A = \frac{1}{J}\left[\left(\frac{\partial y}{\partial\eta} \right)^2 + \left(\frac{\partial x}{\partial\eta} \right)^2 \right], \qquad B = \frac{1}{J}\left(\frac{\partial y}{\partial\xi}\frac{\partial y}{\partial\eta} + \frac{\partial x}{\partial\xi}\frac{\partial x}{\partial\eta} \right),$$
$$C = \frac{1}{J}\left[\left(\frac{\partial y}{\partial\xi} \right)^2 + \left(\frac{\partial x}{\partial\xi} \right)^2 \right]. \tag{C.17}$$

and

$$F^1 = \left(A\varphi_\xi - B\varphi_\eta \right), F^2 = \left(C\varphi_\eta - B\varphi_\xi \right) \tag{C.18}$$

Therefore, 2 dimensional potential equation in each element(Ω^k) is represented as

$$
\begin{aligned}
&\int_{\xi=-1}^1 \phi F^2 \Big]_{\eta=-1}^1 d\xi + \int_{\eta=-1}^1 \phi F^1 \Big]_{\xi=-1}^1 d\eta \\
&- \int_{-1}^1 \int_{-1}^1 \left(F^1\phi_\xi + F^2\phi_\eta \right) d\xi d\eta = \int_{-1}^1 \int_{-1}^1 s J^k \phi \, d\xi d\eta
\end{aligned} \tag{C.19}
$$

Replacing φ by its polynomial approximation Ψ and ϕ by a piecewise continuous polynomial approximation.

$$\phi^k = \sum_{i,j=0}^{N,M} \phi_{ij}^k l_i(\xi) l_j(\eta) \tag{C.20}$$

The following equations are derived.

$$I_1^k \approx \sum_{i,j} \phi_{i,j}^k \left\{ \int_{\xi=-1}^{1} \left[l_i(\xi) l_j(\eta) F^2 \right]_{\eta=-1}^{1} d\xi + \int_{\eta=-1}^{1} \left[l_i(\xi) l_j(\eta) F^1 \right]_{\xi=-1}^{1} d\eta \right\}$$
$$- \sum_{i,j} \phi_{i,j}^k \left\{ \int_{-1}^{1} \int_{-1}^{1} \left(F^1 l_i'(\xi) l_j(\eta) + F^2 l_i(\xi) l_j'(\eta) \right) d\xi d\eta \right\} \tag{C.21}$$

$$I_2^k \approx \sum_{i,j} \phi_{i,j}^k \left\{ \int_{-1}^{1} \int_{-1}^{1} S l_i l_j \, d\xi d\eta \right\} \tag{C.22}$$

where, l is lagrange basis polynomials.

Applying Gauss Lobatto quadrature,

$$\sum_{i,j} \phi_{i,j}^k \left\{ \left(\nabla^2 \Psi, l_i l_j \right)_N - S_{ij}^k J_{ij}^k \omega_i \omega_j \right\} = 0 \tag{C.23}$$

where ω is the quadrature weight. Finally, 2D potential equation in a domain Ω is represented as

$$\sum_{k=1}^{K} \left(\sum_{i,j} \phi_{i,j}^k \left\{ \left(\nabla^2 \Psi, l_i l_j \right)_N - S_{ij}^k J_{ij}^k \omega_i \omega_j \right\} \right) = 0 \tag{C.24}$$

where

$$\left(\nabla^2 \Psi, l_i l_j \right)_N = - \left\{ \sum_{n=0}^{N} D_{in}^{(\xi)T} F_{nj}^1 \omega_n \omega_j + \sum_{m=0}^{M} D_{im}^{(\eta)T} F_{im}^2 \omega_i \omega_m \right\}$$
$$+ \left[F^1(1, \eta_j) l_i(1) - F^1(-1, \eta_j) l_i(-1) \right] \omega_j + \left[F^2(\xi_i, 1) l_j(1) - F^2(\xi_i, -1) l_j(-1) \right] \omega_i$$

$$\tag{C.25}$$

and by replacing Ψ by a piecewise continuous polynomial approximation

$$\Psi = \sum_{i,j=0}^{N,M} \Psi_{ij}^{k} l_i(\xi) l_j(\eta) \qquad \text{(C.26)}$$

the solution for Ψ_{ij} are computed.

At the element interfaces, second and third terms in the right side of equation (C.25) becomes zero, however on jump/flux interface condition, these terms still remains [26, 27, 28, 29].

Bibliography

[1] C. M. Hightower, B. Y. Salazar Vazquez, S.-W. Park, K. Sriram, J. Martini, O. Yalcin, A. G. Tsai, P. Cabrales, D. M. Tartakovsky, P. C. Johnson, and M. Intaglietta, "Integration of cardiovascular regulation by the blood/endothelium cell-free layer," *WIREs Syst. Biol. Med.*, vol. 3, no. 4, pp. 458–470, 2011.

[2] Peng Kai Ong, Swati Jain, and Sangho Kim, "Temporal variations of the cell-free layer width may enhance NO bioavailability in small arterioles: Effects of erythrocyte aggregation," *Microvasc. Res.*, vol. 81, pp. 303–312, 2011.

[3] R. Ghanem and P. Spanos, *Stochastic Finite Elements: A Spectral Approach*, Springer-Verlag, New York, 1991.

[4] D. Xiu and G. Karniadakis, "The Wiener-Askey polynomial chaos for stochastic differential equations," *SIAM J. Sci. Comput.*, vol. 24, no. 2, pp. 619–644, 2002.

[5] O.M. Knio, H.N. Najm, R.G. Ghanem, et al., "A stochastic projection method for fluid flow: I. basic formulation," *Journal of Computational Physics*, vol. 173, no. 2, pp. 481–511, 2001.

[6] O. Le Maitre, MT Reagan, B. Debusschere, HN Najm, RG Ghanem, and OM Knio, "Natural convection in a closed cavity under stochastic non-boussinesq conditions," *SIAM Journal on Scientific Computing*, vol. 26, no. 2, pp. 375–394, 2004.

[7] D. Xiu, D. Lucor, C.H. Su, and G.E. Karniadakis, "Stochastic modeling of flow-structure interactions using generalized polynomial chaos," *Journal of Fluids Engineering*, vol. 124, pp. 51, 2002.

[8] L. Mathelin, M. Yousuff Hussaini, T.A. Zang, and F. Bataille, "Uncertainty propagation for a turbulent, compressible nozzle flow using stochastic methods," *AIAA journal*, vol. 42, no. 8, pp. 1669–1676, 2004.

[9] G. Petrone, C. de Nicola, D. Quagliarella, J. Witteveen, and G. Iaccarino, "Wind turbine performance analysis under uncertainty," *49th AIAA Aerospace Sciences Meeting including the New Horizons Forum and Aerospace Exposition 4 - 7 January 2011, Orlando, Florida*, 2011.

[10] K.L. Van Buren, M.G. Mollineaux, F.M. Hemez, and S. Atamturktur, "Simulating the dynamics of wind turbine blades: part ii, model validation and uncertainty quantification," *Wind Energy*, 2012.

[11] J. Szumbarski, "Instability of viscous incomressible flow in a channel with transversely corrugated walls," *JOURNAL OF THEORETICAL AND APPLIED MECHANICS-WARSAW-*, vol. 45, no. 3, pp. 659, 2007.

[12] Roya Maboudian, "Surface processes in mems technology," *Surface Science Reports*, vol. 30, no. 6-8, pp. 207 – 269, 1998.

[13] J. Ren, B. Ganapathysubramanian, and S. Sundararajan, "Experimental analysis of the surface roughness evolution of etched glass for micro/nanofluidic devices," *Journal of Micromechanics and Microengineering*, vol. 21, no. 2, pp. 025012, 2011.

[14] W.M. Zhang, G. Meng, and Z.K. Peng, "Random surface roughness effect on slider microbearing lubrication," *Micro & Nano Letters, IET*, vol. 5, no. 5, pp. 347–350, 2010.

[15] C. Kunert, J. Harting, and O.I. Vinogradova, "Random-roughness hydrodynamic boundary conditions," *Physical review letters*, vol. 105, no. 1, pp. 16001, 2010.

[16] M. Bahrami, M.M. Yovanovich, and J.R. Culham, "Role of random roughness on thermal performance of microfins," *Journal of thermophysics and heat transfer*, vol. 21, no. 1, pp. 153–157, 2007.

[17] S. Prentner, DM Allen, L. Larcombe, S. Marson, K. Jenkins, and M. Saumer, "Effects of channel surface finish on blood flow in microfluidic devices," *Microsystem technologies*, vol. 16, no. 7, pp. 1091–1096, 2010.

[18] J.B. Taylor, A.L. Carrano, and S.G. Kandlikar, "Characterization of the effect of surface roughness and texture on fluid flowpast, present, and future," *International journal of thermal sciences*, vol. 45, no. 10, pp. 962–968, 2006.

[19] R. Xiong and J.N. Chung, "Investigation of laminar flow in microtubes with random rough surfaces," *Microfluidics and Nanofluidics*, vol. 8, no. 1, pp. 11–20, 2010.

[20] D. M. Tartakovsky and D. Xiu, "Stochastic analysis of transport in tubes with rough walls," *J. Comput. Phys.*, vol. 217, no. 1, pp. 248–259, 2006.

[21] CH Su and D. Lucor, "Covariance kernel representations of multidimensional second-order stochastic processes," *Journal of Computational Physics*, vol. 217, no. 1, pp. 82–99, 2006.

[22] Yu. N. Lazarev, P. V. Petrov, and D. M. Tartakovsky, "Interface dynamics in randomly heterogeneous porous media," *Adv. Water Resour.*, vol. 28, no. 4, pp. 393–403, 2005.

[23] D. Xiu and D. M. Tartakovsky, "Numerical methods for differential equations in random domains," *SIAM J. Sci. Comput.*, vol. 28, no. 3, pp. 1167–1185, 2006.

[24] G. Lin, A. M. Tartakovsky, and D. M. Tartakovsky, "Uncertainty quantification via random domain decomposition and probabilistic collocation on sparse grids," *J. Comp. Phys.*, vol. 229, pp. 6995–7012, 2010.

[25] Lomize M., *Filtratsiya v Treshchinovatykh Porodakh (in Russian)*, Moscow: Gosenergoizda.

[26] D.A. Kopriva, *Implementing Spectral Methods for Partial Differential Equations: Algorithms for Scientists and Engineers*, springer, 2009.

[27] G.E. Karniadakis and S.J. Sherwin, *Spectral/hp element methods for CFD*, Oxford University Press, USA, 1999.

[28] C.G. Canuto, M.Y. Hussaini, A. Quarteroni, and T.A. Zang, *Spectral methods: evolution to complex geometries and applications to fluid dynamics*, Springer, 2007.

[29] C. Pozrikidis, *Introduction to finite and spectral element methods using MATLAB*, Chapman & Hall/CRC, 2005.

[30] M. Sharan and A. S. Popel, "A two phase model for flow of blood in narrow tubes with increased effective viscosity near the wall," *Biorheology*, vol. 38, pp. 415–428, 2001.

[31] M. Sharan, B. Singh, and P. Kumar, "A two layer model for studying the effect of plasma layer on the delivery of oxygen to tissue using a FEM," *Appl. Math. Model.*, vol. 21, pp. 419–426, 1997.

[32] X. Chen, D. Jaron, K. A. Barbee, and D. G. Buerk, "The influence of radial RBC distribution, blood velocity profiles, and glycocalyx on coupled NO/O2 transport," *J. Appl. Physiol.*, vol. 100, pp. 482–492, 2006.

[33] K. John and A. I. Barakat, "Modulation of ATP/ADP concentration at the endothelial surface by shear stress: Effect of flow-induced ATP release," *Ann. Biomed. Eng.*, vol. 29, pp. 740–751, 2001.

[34] C. Xiang, L. Cao, K. Qin, Z. Xu, and B. M. Chen, "A modified dynamic model for shear stress induced ATP release from vascular endothelial cells," in *Bio-Inspired Computational Intelligence and Applications*, K. Li, M. Fei, G. Irwin, and S. Ma, Eds., vol. 4688 of *Lecture Notes in Computer Science*, pp. 462–472. Springer, Berlin/Heidelberg, 2007.

[35] G. A. Mashour and R. J. Boock, "Effects of shear stress on nitric oxide levels of human cerebral endothelial cells cultured in an artificial capillary system," *Brain Res.*, vol. 842, pp. 233–238, 1999.

[36] T. N. McAllister and J. A. Frangos, "Steady and transient fluid shear stress stimulate NO release in osteoblasts through distinct biochemical pathways," *J. Bone Mineral Res.*, vol. 14, pp. 930–936, 1999.

[37] K. Sriram, B. Y. Salazar Vazquez, O. Yalcin, P. C. Johnson, M. Intaglietta, and D. M. Tartakovsky, "The effect of small changes in hematocrit on nitric oxide transport in arterioles," *Antioxid. Redox Signal.*, vol. 14, no. 2, pp. 175–185, 2011.

[38] S. Kim, R. L. Kong, A. S. Popel, M. Intaglietta, and P. C. Johnson, "A computer-based method for determination of the cell-free layer width in microcirculation," *Microcirculation*, vol. 13, pp. 199–207, 2006.

[39] S. Kim, R. L. Kong, A. S. Popel, M. Intaglietta, and P. C. Johnson, "Temporal and spatial variations of cell-free layer width in arterioles," *Am. J. Physiol. Heart Circ. Physiol.*, vol. 293, pp. H1526–1535, 2007.

[40] P. F. Davies, T. Mundel, and K. A. Barbee, "A mechanism for heterogeneous endothelial responses to flow *in vivo* and *in vitro*," *J. Biomech.*, vol. 28, no. 12, pp. 1553–1560, 1995.

[41] K. A. Barbee, T. Mundel, R. Lal, and P. F. Davies, "Subcellular distribution of shear stress at the surface of flow-aligned and nonaligned endothelial monolayers," *Am. J. Physiol. Heart, Circ.*, vol. 268, no. 4, pp. H1765–H1772, 1995.

[42] R. L. J. Satcher, S. R. Bussolari, M. A. J. Gimbrone, and C. F. J. Dewey, "The distribution of fluid forces on model arterial endothelium using computational fluid dynamics," *J. Biomech Eng.*, vol. 114, pp. 309–316, 1992.

[43] M. C. Mazzoni, P. Borgström, M. Intaglietta, and K. E. Arfors, "Lumenal narrowing and endothelial cell swelling in skeletal muscle capillaries during hemorrhagic shock," *Circ. Shock*, vol. 29, no. 1, pp. 27–39, 1989.

[44] C. Kelley, P. D'Amore, H. B. Hechtman, and D. Shepro, "Microvascular pericyte contractility in vitro: comparison with other cells of the vascular wall," *J. Cell Biol.*, vol. 104, no. 3, pp. 483–490, 1987.

[45] M. Loève, *Probability Theory*, Springer-Verlag, New York, 4th edition, 1977.

[46] D. M. Tartakovsky and C. L. Winter, "Dynamics of free surfaces in random porous media," *SIAM J. Appl. Math.*, vol. 61, no. 6, pp. 1857–1876, 2001.

[47] D.M.Tartakovsky G.E.Karniadakis M. Zayernouri, S.W.Park, "Stochastic smoothed profile method for modeling random roughness in flow problems," *submitted to Computer Methods in Applied Mechanics and Engineering, June 17, 2012*, 2012.

[48] R.J. Adler and J.E. Taylor, *Random fields and geometry*, vol. 115, Springer-Verlag, Berlin, 2007.

[49] M. Shinozuka and G. Deodatis, "Simulation of stochastic processes and fields," *Prob. Engrg. Mech*, vol. 14, pp. 203–207, 1997.

[50] D. Lucor, C.H. Su, and G. Karniadakis, "Karhunen-loeve representation of periodic second-order autoregressive processes," *Computational Science-ICCS 2004*, pp. 827–834, 2004.

[51] S.W. Park, M. Intaglietta, and D.M. Tartakovsky, "Impact of endothelium roughness on blood flow," *Journal of Theoretical Biology*, vol. 300, pp. 152–160, 2012.

[52] Mark W. Vaughn, Lih Kuo, and James C. Liao, "Estimation of nitric oxide production and reaction rates in tissue by use of a mathematical model," *Am. J. Physiol. Heart Circ. Physiol.*, vol. 274, pp. 2163–2176, 1998.

[53] Bumseok Namgung, Peng Kai Ong, Paul C. Johnson, and Sangho Kim, "Modulation of NO bioavailability by temporal variation of the cell-free layer width in small arterioles," *Ann. Biomed. Eng.*, vol. 39, pp. 359–366, 2011.

[54] Mark W. Vaughn, Lih Kuo, and James C. Liao, "Effective diffusion distance of nitric oxide in the microcirculation," *Am. J. Physiol. Heart Circ. Physiol.*, vol. 274, pp. 1705–1714, 1998.

[55] Kathleen A. Lamkin-Kennard, Dov Jaron, and Donald G. Buerk, "Impact of the Fahraeus effect on NO and O2 biotransport: A computer model," *Microcirculation*, vol. 11, pp. 337–349, 2004.

[56] Mahendra Kavdia and Aleksander S. Popel, "Wall shear stress differentially affects NO level in arterioles for volume expanders and Hb-based O2 carriers," *Microvasc. Res.*, vol. 66, pp. 49–58, 2003.

[57] Peter Condorelli and Steven C. George, "Free nitric oxide diffusion in the bronchial microcirculation," *Am. J. Physiol. Heart. Circ. Physiol.*, vol. 283, pp. 2660–2670, 2002.

[58] Judith Martini, Benoit Carpentier, Adolfo Chávez Negrete, John A. Frangos, and Marcos Intaglietta, "Paradoxical hypotension following increased hematocrit and blood viscosity," *Am. J. Physiol. Heart Circ. Physiol.*, vol. 289, pp. 2136–2143, 2005.

[59] Maithili Sharan, Balbir Singh, and Pawan Kumar, "A two-layer model for studying the effect of plasma layer on the delivery of oxygen to tissue using a finite element method," *Appl. Math. Modell.*, vol. 21, pp. 419–426, 1997.

[60] A.G. Tsai, B. Friesenecker, M. McCarthy, H. Sakai, and M. Intaglietta, "Plasma viscosity regulates capillary perfusion during extreme hemodilution in hamster skinfold model," *American Journal of Physiology-Heart and Circulatory Physiology*, vol. 275, no. 6, pp. H2170–H2180, 1998.

[61] Bumseok Namgung, Swati Jain, and Sangho Kim, "Effect of cell-free layer variation on arteriolar wall shear stress," *Ann. Biomed. Eng.*, vol. 39, pp. 1012–1023, 2011.

[62] Anthony J. Kanai, Harold C. Strauss, George A. Truskey, Anne L. Crews, Saul Grunfeld, and Tadeusz Malinski, "Shear stress induces ATP-independent transient nitric oxide release from vascular endothelial cells, measured directly with a porphyrinic microsensor," *Circulat. Res.*, vol. 77, pp. 284–293, 1995.

[63] Allison M. Andrews, Dov Jaron, Donald G. Buerk, Patrick L. Kirby, and Kenneth A. Barbee, "Direct, real-time measurement of shear stress-induced nitric oxide produced from endothelial cells in vitro," *Nitric Oxide*, vol. 23, pp. 335–342, 2010.

[64] K. A. Barbee, P. F. Davies, and R. Lal, "Shear stress-induced reorganization of the surface topography of living endothelial cells imaged by atomic force microscopy," *Circulat. Res.*, vol. 74, pp. 163–171, 1994.

[65] M. Sato, K. Nagayama, N. Kataoka, M. Sasaki, and K. Hane, "Local mechanical properties measured by atomic force microscopy for cultured bovine endothelial cells exposed to shear stress," *J. Biomech.*, vol. 33, no. 1, pp. 127–135, 2000.

[66] S. Kim, R. L. Kong, A. S. Popel, M. Intaglietta, and P. C. Johnson, "A computer-based method for determination of the cell-free layer width in microcirculation," *Microcirculation*, vol. 13, pp. 199–207, 2006.

[67] S. Kim, R. L. Kong, A. S. Popel, M. Intaglietta, and P. C. Johnson, "Temporal and spatial variations of cell-free layer width in arterioles," *Am. J. Physiol. Heart Circ. Physiol.*, vol. 293, pp. H1526–1535, 2007.

[68] J. Pittner, M. Wolgast, D. Casellas, and A.E.G. Persson, "Increased shear stress–released no and decreased endothelial calcium in rat isolated perfused juxtamedullary nephrons," *Kidney international*, vol. 67, no. 1, pp. 227–236, 2005.

[69] D. M. Tartakovsky and D. Xiu, "Stochastic analysis of transport in tubes with rough walls," *J. Comput. Phys.*, vol. 217, no. 1, pp. 248–259, 2006.

[70] L. Kuo, W.M. Chilian, and M.J. Davis, "Coronary arteriolar myogenic response is independent of endothelium.," *Circulation research*, vol. 66, no. 3, pp. 860–866, 1990.

[71] J. Zhang, P.C. Johnson, and A.S. Popel, "Effects of erythrocyte deformability and aggregation on the cell free layer and apparent viscosity of microscopic blood flows," *Microvascular research*, vol. 77, no. 3, pp. 265–272, 2009.

[72] R. Ghanem and P. Spanos, *Stochastic Finite Elements: A Spectral Approach*, Springer-Verlag, New York, 1991.